Politecnico di Torino

Laurea Magistrale in

INGEGNERIA DEI MATERIALI PER L'INDUSTRIA 4.0

Collegio di Ingegneria Chimica e dei Materiali

A.a. 2024/2025

Ottobre

Directed Energy Deposition of Ti-Grade 21S: microstructure, mechanical properties and Corrosion behaviour.

Supervisor:

Prof. Abdollah Saboori

Candidate:

Alireza Sohrabi

Acknowledgement

I would like to extend my deepest gratitude to Professor Abdollah Saboori, whose unwavering support, remarkable patience, and constant faith in my abilities have profoundly shaped this journey. From the very beginning, he recognized potential in me often before I recognized it myself and gave me the freedom and encouragement to grow into it. His guidance has been a source of inspiration not only in my academic pursuits but also in my personal development. I will always remain grateful for the trust he placed in me, the invaluable lessons he imparted, and the confidence he helped me build.

I am also sincerely thankful to the Integrated Additive Manufacturing (IAM) Center, under the leadership of Professor Luca Iuliano, for fostering an innovative and collaborative environment that has greatly enriched my research experience. My appreciation extends to the Politecnico di Torino, the Department of Applied Science and Technology, and its dedicated faculty members, whose outstanding academic environment provided the foundation for my growth.

To my family, your unconditional love, patience, and encouragement have been the true cornerstone of this achievement. Your support has continually reminded me of my strength and given me the perseverance to keep moving forward.

Finally, I would like to acknowledge the generous support and contributions of many individuals who believed in me throughout this journey. In particular, I am grateful to Dr. Mohammad Hossein Mosalaneja, Dr. Amir Behjat, Prof. Arash Fattah Alhosseini, Dr. Razieh Charmahali, Dr. Mohammad Taghian and Amir Hossein Movahedian for their guidance and encouragement along the way.

This work is the result of the collective kindness, mentorship, and belief of all those who stood beside me, and I feel truly fortunate to have shared this path with you.

Abstract

Metastable β-titanium alloys are attractive for the aerospace industry and medical applications, due to their low density, high strength, low young modulus, and excellent hardenability. Among these alloys, Titanium Grade 21S is renowned for its outstanding elevated temperature strength, creep resistance, corrosion resistance and mechanical properties. However, its limited weldability and poor thermal conductivity present significant challenges to traditional manufacturing methods, resulting in increased difficulty and costs. This study explores the potential of laser powder directed energy deposition (LP-DED) to fabricate Ti-21S samples. This additive manufacturing (AM) technique as compare to other fusion-based AM processes, offers faster material deposition rates, resulting in faster build times. The produced components were comprehensively evaluated for their microstructure, mechanical properties, and corrosion behavior using various methodologies. Based on the defect analysis, it was achieving >99.9% of theoretical density with appropriate processing parameters. Microstructure analysis indicated a fully beta-phase microstructure alongside notable mechanical strength and corrosion resistance. Hardness and microstructural uniformity were consistent across all samples, while electrochemical tests demonstrated robust resistance to aggressive environments. These findings underscore the effectiveness of LP-DED as a processing technique for Ti-21S, preserving its advantageous properties and addressing the limitations of conventional manufacturing.

Keywords: Beta-Ti21S alloy, Laser powder directed energy deposition, Additive manufacturing, Materials characterization, medical applications.

Table of Contents

Table of Tables

Table of Figures and Diagrams

Table of Abbreviations

AM	Additive Manufacturing
Bcc	Body-Centered Cubic
DED	Directed Energy Deposition
EB-PBF	Electron Beam Powder Bed Fusion
Hcp	Hexagonal Close-Packed
HT	Heat Treatment
OM	Optical Microscope
L-PBF	Laser Powder Bed Fusion
PBF	Powder Bed Fusion
Ra	Arithmetic Mean Surface Roughness
Rz	Average Height of the Profile
Ti6Al4V (Ti64)	Titanium-6Aluminum-4Vanadium
Ti21S	Titanium-15Molybdenum-3Aluminum-3Niobium-0.2Silicon

1. Introduction

1.1. State of the Art

Titanium alloys are widely recognized for their excellent corrosion resistance, high specific strength, and outstanding biocompatibility. These properties have enabled their use in diverse fields such as biomedical implants [1], [2], aerospace[2], automotive[3], and high-temperature applications where both creep resistance and corrosion behavior are critical[4]. Despite these advantages, their widespread adoption is hindered by two main factors: the high cost of titanium [5], [6] and the limitations of conventional manufacturing methods such as casting, rolling, and forging. The strong reactivity of molten titanium with mold materials has made conventional casting particularly challenging and thus rarely applied [7].

In recent years, additive manufacturing (AM) has emerged as a promising approach for processing titanium alloys. Nevertheless, research in this area has largely been concentrated on the Ti-6Al-4V alloy[8]. While Ti-6Al-4V has demonstrated significant potential in high-temperature environments, its behavior and capabilities in AM processes remain insufficiently explored. Other titanium alloys, such as Ti-21S, have received limited attention in comparison[9]

In addition to cost and processing difficulties, titanium alloys also present challenges during machining and forming. Their low thermal conductivity leads to high cutting temperatures, complicating machining operations [10][11]. Furthermore, their pronounced spring-back behavior makes cold forming difficult, even after annealing[12], [13]. Another drawback of Ti-6Al-4V for biomedical use is its relatively high elastic modulus compared to human bone, which can contribute to stress shielding. This issue is of growing concern given the rapidly aging global population, highlighting the need for alternative titanium alloys with improved biomedical compatibility [14].

Industries are therefore increasingly turning to additive manufacturing techniques as a means to reduce production costs, shorten lead times, and at the same time exploit the superior properties of titanium alloys[15].Titanium feedstock is generally available in powder and wire form, enabling the use of different AM technologies [15], [16]. The most established methods for processing titanium alloys are directed energy deposition (DED) and powder bed fusion (PBF). PBF includes both laser powder bed fusion (L-PBF) and electron beam powder bed fusion (EB-PBF), while DED involves the use of a laser, electron beam, or electric arc to melt powder or wire feedstock as it is deposited along programmed paths [17], [18]. This study focuses on the mechanical behavior, microstructure, and corrosion properties of additively manufactured titanium alloys, with a comparative evaluation of Ti-6Al-4V and Ti-21S.

1.2. Titanium Alloys

In recent years, considerable research has focused on advancing materials tailored for biomedical, aerospace, and automotive industries[19]. A variety of metallic materials, such as steels, cast iron, nickel-based alloys, and other metals known for their exceptional mechanical properties, have been documented for use in manufacturing within these sectors[20]. Nevertheless, titanium and its

alloys have emerged as particularly exceptional choices due to their enhanced characteristics Titanium alloys are composite materials primarily composed of the element titanium, which is combined with other elements such as aluminum, vanadium, and nickel to enhance its properties. These alloys are engineered to take advantage of the unique characteristics of titanium, which include its exceptional strength-to-weight ratio, corrosion resistance, and biocompatibility[21], [22].

Titanium alloys are excellent options for Additive Manufacturing (AM), and significant efforts have been made to enhance the applications of this technology[23], Titanium alloys can be further categorized into different classes or groups based on their composition and properties. Some of the common classes of titanium alloys include; α-titanium (α-Ti) and pure titanium (cp-Ti) exist in the alpha phase at temperatures below 882.5°C, characterized by a hexagonal crystal lattice structure. When the temperature exceeds 883°C, titanium alloy transitions to the beta phase[24]. They are often used in applications where corrosion resistance is critical, such as chemical processing equipment. The second class is related to (β-Ti), The beta type contains a significant amount of beta stabilizers in Cp-Ti and titanium alloys, which prevents the formation of intermetallic compounds like Mo, Ta, Zr, etc. Additionally, beta type titanium alloys can undergo heat treatment, which enhances their endurance strength.They are used in applications that require elevated temperature performance, like aircraft engine components. Another class (α + β Ti), which is a dual-phase α + β alloy, The (α + β) phase in cp-Ti forms when the temperature exceeds 882.5°C. Additionally, the (α + β) phase in cp-Ti exhibits moderate strength at elevated temperatures which is used extensively in the aerospace industry due to its high specific strength, and high specific stiffness[20]. The phase diagram of Titanium will show in Figure1.

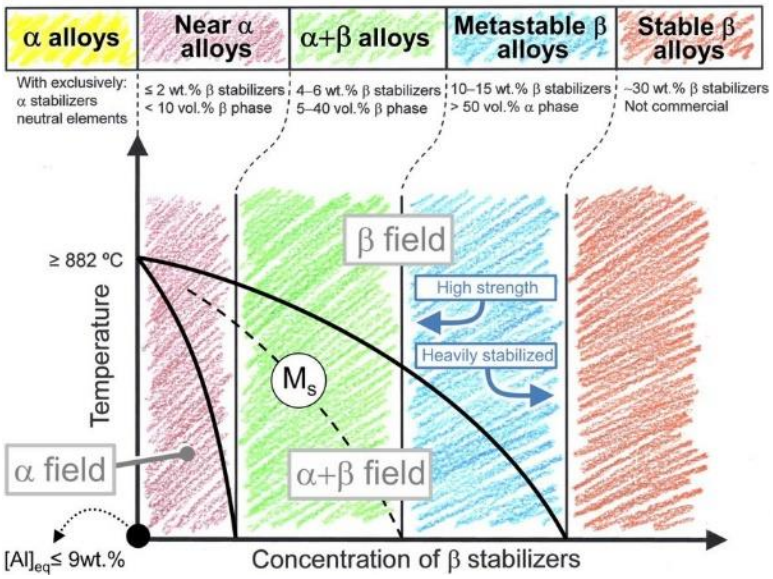

Figure 1. Phase diagram of the titanium alloys [9]

1.3. Beta Titanium alloys

β-Ti alloys refer to titanium alloys in which the β-phase remains substantially stable either in equilibrium or upon rapid cooling from the β-phase without converting into martensite or the α-phase. Additionally, these alloys typically incorporate non-toxic elements like tantalum, niobium, molybdenum, tin, and zirconium to obtain β-Ti alloys that are biocompatible[25]. According to the above, β-Ti alloys, due to their applications can be used in different areas of work such as the medical field.

Titanium and its alloys are commercially important for many industries. They are used for engineering applications in the aerospace industry, the biomedical and healthcare Industry, the energy and power generation industry, and the petrochemical industry [26].

Beta titanium alloys, known for their high strength and excellent corrosion resistance, are increasingly utilized in various advanced engineering applications, including aerospace and medical devices. A critical factor in optimizing the performance of these alloys is the use of beta titanium stabilizers [27] that are completely shown in Figure2.

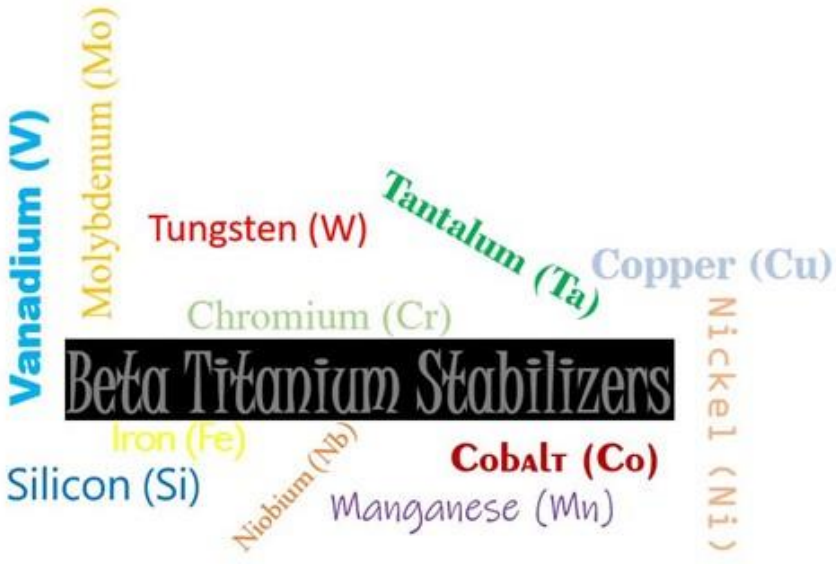

Figure 2. Beta Stabilizing Elements

Beta titanium alloys are a class of titanium materials distinguished by their high strength, excellent corrosion resistance, and superior formability. These alloys, characterized by the presence of beta-stabilizing elements which was shown in Figure 2, exhibit a body-centered cubic (Bcc) crystal structure at room temperature. The unique properties of beta titanium alloys make them ideal for a wide range of high-performance applications, including aerospace, medical implants, automotive, and chemical processing industries. Table 1 will show the different grades of this class.

Table 1. Different grades of Beta Ti alloys [21], [25], [26], [27], [28]

Beta Titanium Grades			
1	Ti-13V-11C-3Mo (also known as B120VCA)	2	Ti– 1Al – 8V–5Fe 1 –8– 5 Metastable (19)
3	Ti– 13V– 11Cr –3Al B120 VCA Metastab (23)	4	Ti– 12Mo –6Zr –2Fe TMZF
5	Ti-10V-2Fe-3Al (Ti1023) TB6	6	Ti– 4.5Fe– 6.8Mo –1.5Al TIMETAL
7	β-21S (Ti-15Mo-3Al-3Nb-0.2Si)	8	Ti– 15V– 3Cr–1Mo –.5Nb –3Al – 3Sn– .5Zr VT35
9	Ti-3Al-8V-6Cr-4Mo-4Zr (Beta-C) ASTM Grade 19, (Ti-38644)	10	Ti– 3Al – 8V–6Cr–4Mo– 4Zr Beta-C
11	Ti-1Al-8V-5Fe (Ti-185)	12	Ti– 15Mo
13	Ti-35Nb-7Zr-5Ta	14	Ti– 8V –8Mo–2Fe– 3Al
15	Ti-24Nb-4Zr-8Sn OR Ti2448	16	Ti– 15Mo –2.6Nb– 3Al –0.2Si
17	Ti-35Zr-28Nb	18	Ti– 11.5Mo –6Zr –4.5Sn
19	Ti–29Nb–13Ta–4.6Zr	20	Ti– 10V– 2Fe –3Al
21	Ti–15Mo–5Zr–3Al (Ti-1553)	22	Ti– 5V –5Mo–1Cr –1Fe–5Al
23	Ti-13V-11Cr-3Al (Ti-13113)	24	Ti– 5Al – 2Sn –2Zr –4Mo –4Cr
25	Ti-13V-2Fe-3Al (Ti-1323), Beta super elastic	26	Ti– 4.5Al –3V– 2Mo– 2Fe
27	Ti– 35V– 15Cr (Alloy C, Beta (47))	28	Ti– 5Al – 2Sn –2Cr –4Mo–4Zr Beta CEZ Beta-rich
29	Ti– 40Mo (Beta (40))	30	Ti– 13Nb –13Zr
31	Ti– 30Mo (Beta (30))	32	Ti–12Mo
33	Ti– 6V-6Mo – 5.7Fe– 2.7Al TIMETAL 125 Metastab (24)	34	Ti-25Nb-3Zr-3Mo-2Sn
35	Ti– 15V– 3Cr–3Sn–3Al		

Moreover, one of the important issues in manufacturing beta titanium alloy is the complexity of the product that should be solved, and one of the best ways to produce complex part designs is Additive Manufacturing.

Additive manufacturing (AM), commonly referred to as 3D printing, is a manufacturing technique that constructs parts layer by layer using materials such as powder, wire, or sheets [29]. All of the metal AM technologies are based on the concept of slicing a solid model into multiple layers to create a tool path, this model can be designed by CAD software, uploading these data into the machine, and building the part up, layer by layer, following the sliced model data, using a heat source (laser, electron beam or electric arc) and feedstock (metal powder or wire)[30].

Additionally, the production of components in this field presents a level of complexity that cannot be addressed by traditional manufacturing techniques. For example, certain complex components manufactured using additive manufacturing (AM) in the medical industry include custom implants, prosthetics, and surgical instruments. These components are often designed with intricate geometries tailored to individual patients, which would be challenging or impossible to achieve using traditional manufacturing methods (Figure 3).

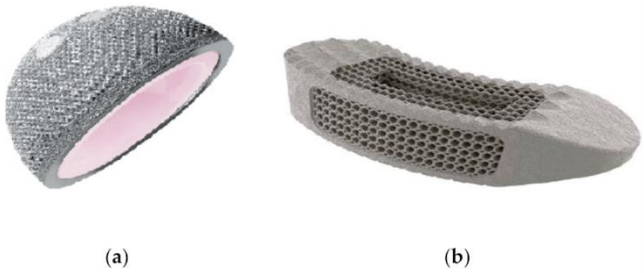

Figure 3. Dental and Medical additive manufactured components: (a) titanium-alloy orthopaedic device [15], and (b) porous titanium spinal implant

As a result, scientists and engineers have sought alternative methods for fabricating intricate parts. Among the available technologies, Additive Manufacturing (AM) stands out for its ability to build complex structures through a layer-by-layer approach, making it particularly appealing to various industries. Despite the growing interest in this area, there is a noticeable lack of comprehensive reviews focusing on the additive manufacturing of beta-titanium alloys[31], particularly in terms of mechanical properties and microstructure. To fill this gap, we have undertaken this work to examine the processability of beta-titanium alloys and highlight the most recent advancements in the field.

1.4. Ti-21S

1.4.1. History

The β-Ti21S alloy is a metastable beta titanium alloy characterized by a high specific strength and excellent cold formability[32]. It was specifically developed to provide superior oxidation resistance, thermal stability, high-temperature strength, and corrosion resistance. An earlier alloy, Ti-15V-3Cr-3Sn-3Al , had been designed primarily for foil applications and evaluated for service at temperatures above 815 °C; however, it demonstrated significant susceptibility to oxidation under such conditions. To overcome these limitations, Timet introduced the β-Ti21S alloy in 1989, with the goal of enhancing the oxidation resistance of metal-matrix composites (MMCs) used by McDonnell Douglas for the National Aerospace Plane (NASP) program[33].

1.4.2. Chemistry and Metallurgy

The chemical composition of the β-Ti 21S alloy was carefully engineered to enable cost-effective forming processes. Its design emphasized high processability and reduced labor requirements, which made production more economical. Specifically, this metastable β alloy was optimized for the manufacture of thin foil products through extensive cold rolling [34]. The Ti-V system, represented by alloys such as Ti-15V-3Cr-3Sn-3Al and Ti-3Al-8V-6Cr-4Zr-4Mo, was already well established and widely applied in metastable β alloys. However, vanadium-based systems suffer from poor oxidation resistance. For this reason, the development strategy shifted toward vanadium-free systems, particularly those based on Ti-Mo and Ti-Cr.

Systematic alloying studies within the Ti-Mo system demonstrated that elements such as aluminum, iron, silicon, niobium, tantalum, palladium, and hafnium significantly improved oxidation resistance, whereas additions of tin, zirconium, cobalt, or yttrium were ineffective. Furthermore, it was determined that increasing the Mo content above 15 wt.% offered no additional benefit. In contrast, alloying failed to improve the corrosion resistance of Ti-Cr alloys. Based on these findings, the final composition of β-Ti21S (as presented in Table 2) was established. Modified versions of this alloy were also developed: one with palladium additions to provide exceptional resistance to stress corrosion, and another without aluminum to meet the requirements of orthopedic applications.[34].

Table 2. The chemical composition of β-Ti21S (wt.%)[34].

Composition, wt.%										
Element	Mo	Nb	Al	Si	Fe	C	O_2	N_2	H_2	Ti
Minimum	14.0	2.4	2.5	0.15	0.2	…	0.11	…	…	…
Maximum	16.0	3.0	3.5	0.25	0.4	0.05	0.15	0.05	0.015	…
Aim	15.0	2.8	3.0	0.20	0.3	…	0.13	…	…	bal

The β-stabilizing elements in β-Ti21S include approximately 12.8 wt.% molybdenum, which classifies this material as a metastable β-titanium alloy. Molybdenum and niobium act as the primary β stabilizers. Aluminum, although typically known as an α-stabilizing element, is also present in a significant proportion. In this alloy, aluminum contributes to solid-solution strengthening but at the expense of ductility. Its main function, however, is to accelerate the precipitation kinetics of the α-phase during aging treatments while suppressing the formation of the undesirable isothermal ω-phase [14]. Aluminum additions also lower the martensitic transformation start temperature (Ms).

Silicon is intentionally added in small amounts to enhance corrosion and creep resistance. Nevertheless, excess silicon content can reduce ductility. In titanium alloys, silicon remains in solid solution up to about 0.10 wt.% and beyond that tends to precipitate at grain boundaries as silicides. These fine silicide particles inhibit grain-boundary motion, strengthen α/β interfaces at elevated temperatures, and act as preferential nucleation sites for grain-boundary α precipitation during heat treatment. Importantly, these silicides dissolve completely at approximately 1025 °C. Iron, classified as a β-eutectoid stabilizer, is generally regarded as an impurity. While its addition is cost-effective, it introduces significant drawbacks: it broadens the solidification temperature range, promotes severe microsegregation that is difficult to eliminate even with homogenization heat treatments, and its high diffusion rate adversely affects creep resistance[14], [24].

Light interstitial elements such as carbon, oxygen, and nitrogen mainly strengthen the α-phase through solid-solution hardening; however, their concentrations must be strictly controlled. Oxygen, for example, must remain below 0.25 wt.% because higher levels negatively affect the strength-ductility balance in both annealed and aged conditions. In the annealed state, oxygen decreases work-hardening ability and increases the tendency for localized necking, while in the aged condition it promotes brittleness by facilitating the precipitation of α-phase along grain boundaries, leading to intergranular fracture. For these reasons, the oxygen level in β-Ti21S is

restricted to about 0.17 wt.%. Consequently, manufacturing and heat treatment of β-Ti21S require careful control to avoid the formation of unwanted phases associated with impurity elements, making processing more complex and costly [14], [24], [29], [32], [35].

Table 3. Ti 21S data sheet.

General Information	
Property	Description
Alloy designation	Ti-21S (Beta Titanium Alloy)
UNS number	R58210
Product forms	Bar, Plate, Sheet, Forging, Wire
Microstructure	Metastable Beta alloy
Chemical Composition (wt.%)	Ti (Balance), Mo 15.0, Nb 2.7, V 3.0, Al 0.2, Si 0.06
Physical Properties	
Density	4.94 g/cm³
Melting range	~1660–1710 °C
Elastic modulus (E)	~105 GPa
Thermal conductivity	~6.7 W/m·K
Specific heat	~0.54 J/g·K
Mechanical Properties (Annealed)	
Tensile strength (UTS)	~1100 MPa
Yield strength (0.2% offset)	~1035 MPa
Elongation	~10–15 %
Hardness	~340 HV
Fatigue strength (R = –1)	~600 MPa
Processing & Applications	
Heat treatment	Solution treatment + aging to enhance strength
Workability	Good forgeability in beta phase
Weldability	Moderate, requires shielding
Machinability	Similar to other beta Ti alloys
Applications	Aerospace structures, landing gear, fasteners, biomedical implants

1.5. Additive Manufacturing (AM)

Additive Manufacturing (AM) is an automated, layer-by-layer fabrication technique used to produce three-dimensional physical components directly from CAD models, without the need for part-specific tooling. Initially introduced under the name “3D Printing”, this term is still widely used today. Together with the well-established fields of Subtractive Manufacturing (e.g., milling, turning) and Formative Manufacturing (e.g., casting, forging), Additive Manufacturing forms the third fundamental pillar of modern manufacturing technology. When AM first appeared on the market in 1987, it was referred to as “Rapid Prototyping” or “Generative Manufacturing”. Although these names are still occasionally used, over the years numerous additional terms have been introduced, many of them originating from specific companies or technologies. While each

designation reflects the perspective of its creator, this proliferation of terminology has often led to confusion, particularly for newcomers entering the AM field.

Since AM is a relatively recent technology, standardization efforts were limited in its early years, apart from preliminary initiatives in Germany during the early 1990s. In 2007, the German Association of Engineers (VDI) introduced the guideline VDI 3404, which was published the following year. Shortly after, in 2009, the American Society of Mechanical Engineers (ASME) in collaboration with ASTM International began developing standardized frameworks. Later that year, the ASTM Committee F42 on Additive Manufacturing (subcommittee F42.91 on Terminology) released the ASTM F2792-09e1 standard, also known as the Standard Terminology for Additive Manufacturing Technologies. This document formally defined the term “Additive Manufacturing”. Despite these advancements, widespread adoption of standardized terminology has taken time, and a variety of terms often driven by brand names or company-specific usage continue to coexist, sometimes even competing with one another.

At its core, Additive Manufacturing is an evolving automated process based on the principle of layer-wise fabrication. The process begins with a three-dimensional CAD model of the part to be manufactured. In engineering practice, this digital model can be created through 3D CAD software, 3D scanning, or imaging methods such as computed tomography (CT). Regardless of how it is generated, the model is converted into a series of two-dimensional cross-sectional slices using specialized software. This slicing process yields data consisting of the x–y contour, the defined layer thickness (Δz), and the corresponding z-coordinate for each layer.

The processed data are then transmitted to the AM machine, which builds the component layer by layer. Each layer is formed through two fundamental steps: deposition of material in accordance with the defined cross-sectional geometry, and subsequent solidification or bonding of that material. By repeating these steps iteratively, the full three-dimensional part is produced.

The mechanical properties of metallic biomaterials are of critical importance because these materials must meet strict performance requirements within the complex physiological environment of the human body[36]. It is well established that properties measured under in vivo conditions may be considerably lower than those obtained under standard laboratory testing[37]. These characteristics are strongly dependent on the processing route, as the manufacturing method dictates the final microstructure, which in turn governs the mechanical behavior [38].

Conventional manufacturing techniques such as casting and machining present limitations when producing components for biomedical applications. Titanium and its alloys, in particular, are difficult to process due to their high reactivity at elevated temperatures[39]. Producing high-quality titanium components typically requires vacuum casting to prevent contamination. Furthermore, machining these alloys is challenging because of their low thermal conductivity, which leads to excessive heat generation and galling (adhesive wear between contact surfaces) [40]. High-speed machining with appropriate cooling is therefore necessary[41]. Titanium and its alloys also exhibit high strain-rate sensitivity, complicating plastic deformation processes such as forging and rolling[42].

The polymorphic nature of titanium introduces further complexity in processing. The temperature at which the allotropic transformation (β-transus) occurs depends on the alloying elements present[43], [44]. While β-phase alloys can undergo substantial thickness reductions (up to 90%) through rolling, α and near-α alloys display limited formability at low temperatures, whereas α+β alloys demonstrate better workability[45], [46]. As a result, the microstructure has a decisive influence on deformation behavior and work-hardening rates. Ti-6Al-4V, the most widely used α+β alloy, is characterized by very high flow stress at room temperature, resulting in poor cold formability[47]. Although cold processing avoids contamination, high-temperature processing increases the risk of oxygen and hydrogen pickup, which can cause embrittlement. To enhance formability, forging is typically carried out close to the β-transus temperature (~980 °C), where the abundance of slip systems in the β-phase facilitates deformation. However, at temperatures above 600 °C, the protective oxide layer on titanium is disrupted, exposing the metal to oxidation and surface degradation. Consequently, forging at these high temperatures requires a carefully controlled environment to avoid contamination, which adds significantly to the production cost. While wrought titanium alloys exhibit superior mechanical properties compared to cast alloys, forging and subsequent machining remain complex and expensive manufacturing routes [48].

Additive manufacturing (AM) has recently emerged as an innovative alternative for producing complex and patient-specific biomedical components. By integrating digital design tools, such as medical imaging, AM enables the fabrication of customized implants tailored to individual anatomical requirements. Although AM is more expensive than conventional techniques, these costs are offset by the benefits it offers, including individualized treatment, reduced surgical time, faster recovery, and decreased overall burden on healthcare systems. Furthermore, AM makes it possible to design porous structures that significantly lower the elastic modulus of titanium components, bringing it closer to that of natural bone and reducing the risk of stress shielding, while also decreasing the overall weight of the implant[49].

AM encompasses a family of technologies that build three-dimensional components layer by layer, contrasting with traditional formative methods such as casting or plastic deformation. According to the ISO/ASTM 52900:2015 standard, AM processes are classified into seven main categories. Among these, powder bed fusion (PBF) has become the most widely adopted method in the biomedical sector[50]. In PBF, thermal energy selectively melts regions of a thin powder layer to consolidate material. Depending on the heat source, PBF is subdivided into laser powder bed fusion (L-PBF) [51]and electron beam powder bed fusion (E-PBF)[52]. In L-PBF, a laser beam selectively scans the powder bed under an inert gas atmosphere, whereas in E-PBF, an electron beam operates in a vacuum, following a preheating step (typically 600–700 °C for titanium alloys). These two approaches differ in their cooling rates, E-PBF has a lower cooling rate due to the preheating, resulting in different solidification conditions, microstructures, and final properties. While extensive research has been devoted to the AM of Ti-6Al-4V, studies on the additive manufacturing of biocompatible β-titanium alloys remain comparatively scarce[53].

1.5.1. PBF

Powder Bed Fusion (PBF) technologies employ a focused energy source either an electron beam or a laser to selectively melt localized regions of a thin layer of pre-deposited powder, enabling the layer-by-layer fabrication of three-dimensional components [54]. Depending on the type of

energy source applied, PBF processes are classified into two principal categories: Electron Beam Powder Bed Fusion (EB-PBF) and Laser Powder Bed Fusion (L-PBF)[55].

In both techniques, the build process begins with the uniform spreading of a thin layer of metal powder over the build platform. The energy beam then selectively scans and melts specific regions according to the cross-sectional data extracted from a computer-aided design (CAD) model. After the solidification of each scanned layer, the build platform is lowered, and a new powder layer is deposited, repeating the cycle until the entire component is completed[56].

While the fundamental principles are similar, the two methods differ significantly in terms of operating environment, heat source, and resulting microstructures. L-PBF uses a high-intensity laser under an inert gas atmosphere, which enables very fine feature resolution and precise geometries. However, the process often leads to steep thermal gradients, which can result in residual stresses and anisotropic properties in the final component. In contrast, EB-PBF employs a high-energy electron beam in a vacuum chamber. This approach allows the build area to remain at elevated temperatures throughout the process, thereby reducing residual stresses, mitigating cracking in sensitive alloys, and enabling the production of near-fully dense parts[57].

These PBF-based additive manufacturing techniques are increasingly recognized for their capability to produce complex geometries, lightweight structures, and customized parts that are challenging or impossible to achieve through conventional manufacturing methods[58]. Consequently, they are gaining prominence in aerospace, biomedical, and high-performance engineering applications. Recent research continues to refine PBF parameters such as scanning strategies, beam power, hatch spacing, and layer thickness in order to enhance dimensional accuracy, control microstructure, and improve the mechanical performance of additively manufactured components. Furthermore, there is growing interest in integrating PBF processes with advanced modeling and simulation tools, which will further accelerate the development of functionally graded materials and multi-material structures in the near future[59].

1.5.2. L-PBF

Laser Powder Bed Fusion (L-PBF) is among the most prominent additive manufacturing techniques, enabling the fabrication of components with highly complex internal architectures and unconventional geometries [60], [61]. In this process, a thin layer of metal powder is evenly distributed across a build platform [62], after which a high-energy laser beam selectively melts the material in accordance with the CAD model. Once a layer is completed, the build platform is incrementally lowered, allowing the next layer of powder to be deposited and fused. This sequence of deposition and selective melting is repeated layer by layer until the entire part is completed[63].

The key process parameters that govern L-PBF include laser power, scan speed, hatch spacing, and layer thickness (Figure 4) [64]. Additionally, varying scanning strategies and parameter settings in different regions of the component or support structures allow the production of intricate and tailored designs[65].

Due to the use of a highly focused laser beam operating at high scan speeds, L-PBF is characterized by extremely rapid cycles of heating, melting, solidification, and cooling. Cooling rates can reach

values as high as 10^6 K/s, resulting in a fine-grained microstructure and, consequently, enhanced mechanical properties. However, the layer-wise build approach and steep thermal gradients can also lead to challenges such as anisotropic microstructures, the presence of residual stresses, and non-uniform porosity [66]. Because the powder is pre-distributed on the substrate, the L-PBF process requires finer powders and less energy to achieve full densification. This enables the use of lower laser powers combined with faster scanning speeds to produce dense parts [67]. Thanks to its high precision and accuracy, L-PBF is particularly well-suited for applications that require complex geometries and excellent surface quality. Moreover, its applicability across a wide range of materials further expands its versatility [68]. The high degree of freedom provided by L-PBF process enables the creation of complex geometries to meet some strategic industry needs:

• light-weighting through topological optimization

• multicomponent systems (e.g., composite)

• tailored gradient structures.

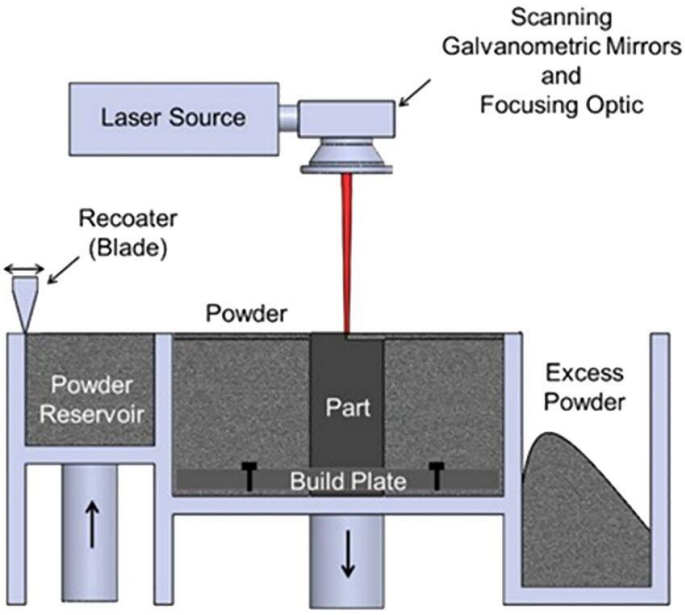

Figure 4. Schematic representation of L-PBF.[67]

1.5.3. EB-PBF

The local melting of the material can be achieved by an electron beam that replaces the laser. The procedure is then called electron beam melting, EBM. Because electron beam material processing requires a vacuum, a completely sealed construction is needed. Arcam AB of Mölndal, Sweden presents a family of EBM machines dedicated to special applications, such as aerospace, medical, or tooling. The electron beam penetrates very deep and the set up allows a very high scan speed that can be used for preheating as well, therefore the process is very fast and works at elevated temperatures. As a result, stress and distortion are reduced and very good material properties can be achieved, according to the company.

In the Electron Beam Powder Bed Fusion (EB-PBF) process, an electron beam serves as the primary heat source. This beam consists of free electrons that are precisely manipulated and directed using electric and magnetic fields, generating a concentrated and high-energy beam within a vacuum environment. When these high-velocity electrons strike the material surface, their kinetic energy is converted into heat, which, when sufficiently localized, is capable of melting electrically conductive materials[69].

The entire EB-PBF process must be carried out inside a vacuum chamber because electrons can be scattered and deflected when they interact with gas molecules between the electron gun and the target material. A vacuum level of 10^{-4} to 10^{-5} mbar is typically maintained, which is particularly critical for processing metals and alloys that are highly sensitive to reactive gases such as oxygen and nitrogen [70]. To further mitigate problems associated with electrostatic charging and the formation of powder "smoke," a low partial pressure of helium, around 10^{-3} mbar, is introduced into the chamber [71].EB-PBF offers specific advantages that enable high productivity, including the ability to produce near-fully dense parts in a single build cycle. After the digital model is sliced, optimized, and uploaded into the machine (as shown in Figure 5), the electron beam preheats the powder bed to an elevated temperature before melting the material through two distinct strategies: contour melting for outlining the geometry and hatch melting for filling the interior. Throughout the build process, the chamber remains at high temperatures often exceeding 1000 °C which significantly minimizes residual stresses and makes it possible to process alloys that are typically susceptible to cracking.

Compared to L-PBF, the EB-PBF process results in substantially lower residual stresses due to its high build temperature. This characteristic allows the fabrication of components with minimal internal stress and distortion, distinguishing EB-PBF as a preferred technique for certain advanced materials [72].

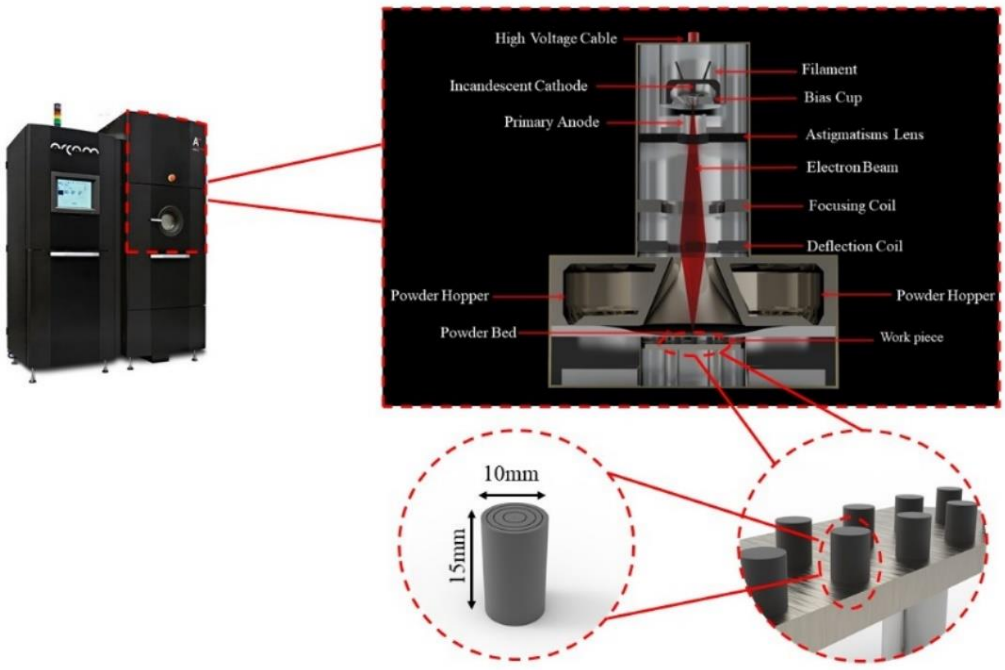

Figure 5. Principal schematic of the EBM machine.

2. Materials & Methods

2.1. Sample Preparation

The Ti-21S specimens were fabricated using the Laser Powder Directed Energy Deposition (LP-DED) process. Before producing the designated samples, a series of printing parameter optimizations was conducted to improve the overall quality and density of the deposited material. This step was crucial because process parameters play a decisive role in determining the porosity and structural integrity of additively manufactured components [73]. Considering the strong affinity of Ti-21S alloy for oxygen, the manufacturing process must be performed in a controlled, low-oxygen environment. For this reason, our collaborators at the University of Applied Sciences and Arts of Southern Switzerland employed a 4D hybrid additive manufacturing system to carry out the sample production under vacuum conditions.

2.1.1. Parameter optimization

In the optimization of L-PBF process parameters, the Design of Experiment (DoE) approach plays a crucial role, as numerous adjustable parameters affect the final build quality. Key factors include laser power, scanning speed, and hatch spacing. In the case of LP-DED (Laser Powder Directed Energy Deposition), a similar concept to the Volumetric Energy Density (VED) used in L-PBF is applied; however, it is typically expressed as Linear Energy Density (LED) because, in this process, the material is deposited in tracks rather than in thin layers of powder.

$$LED = \frac{P}{V.h}$$

where:

P = Laser power (W)

v = Scanning speed or travel speed of the laser (mm/s)

h = Hatch spacing or bead width (mm)

in rare cases, if hatch spacing is not considered (single track), it is simplified to:

$$LED = \frac{P}{V}$$

This formula represents the **energy delivered per unit length** of the deposition path.

The Linear Energy Density (LED) quantifies the amount of energy delivered per unit length of deposited track and is a fundamental parameter for optimizing the LP-DED process. In this study, to achieve optimal manufacturing conditions, a narrow parameter range was selected based on previous research. Specifically, three levels of laser power [400,500 W] and three levels of laser scan speed [500,600 mm/min] were examined, while keeping all other processing parameters constant. Table 3 presents the calculated LED values along with the corresponding parameter combinations.

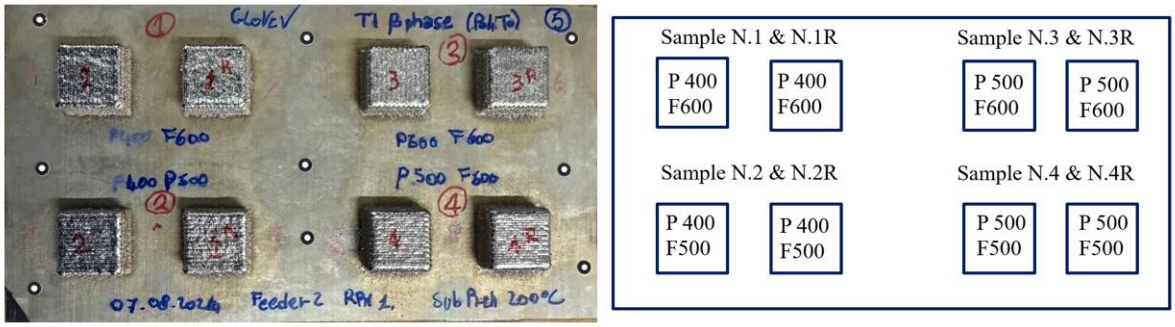

Figure 6. Printed Sample and parameters.

Table 4. Printing parameters for Ti-21S

	Power (W)	Speed (mm/min)	H.D (mm)	Dz (µm)	Raster	LED (J/MM)
S N.1 & N.1R	400	600	0.479	186	0°/ 90°	1.39
S N.2 & N.2R	400	500	0.501	151	0°/ 90°	1.59
S N.3 & N.3R	500	600	0.589	170	0°/ 90°	1.41
S N.4 & N.4R	500	500	0.605	201	0°/ 90°	1.65

2.1.2. DoE sample preparation

In this study, gas-atomized Ti-21S metastable beta titanium powder, with a particle size distribution between 45 μm and 105 μm, was used as the feedstock material. Cubic specimens with dimensions of 20 × 20 × 5 mm³ (length × width × height) were produced using a 4D Hybrid machine. Prior to the start of the deposition process, the build chamber was purged with argon to create an inert atmosphere, minimizing the influence of oxygen during fabrication. As presented in Table 3, four different parameter combinations were employed, with two repetitions for each condition. Additionally, the substrate was preheated to 200 °C before fabrication.

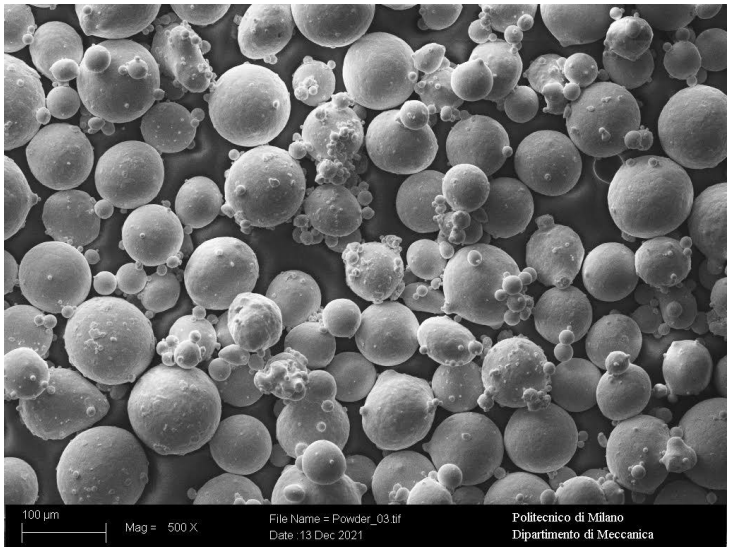

Figure 7. SEM image of gas-atomized Ti-21S metastable beta titanium powder.

2.2. Wire Electrical Discharging Machine (WEDM)

2.2.1. Historical background

Wire Electrical Discharge Machining (WEDM), also known as wire-cut EDM, emerged in the late 1960s as an evolution of the conventional electrical discharge machining (EDM) process. The original EDM technology, first developed in the 1940s by Lazarenko in the Soviet Union, exploited the phenomenon of controlled electrical discharges to machine conductive materials without direct mechanical contact[74]. In 1969, the first commercially viable WEDM systems were introduced in Japan, using a continuously moving thin wire as the electrode instead of a shaped tool. This breakthrough enabled the precise machining of intricate contours, narrow kerfs, and complex profiles in very hard materials[75]. Over the past five decades, WEDM has become an indispensable process in industries such as aerospace, die and mold manufacturing, biomedical engineering, and micro-component fabrication, due to its unique ability to achieve high dimensional accuracy and excellent surface integrity on conductive materials[76].

Figure 8. G.cut WEDM machine.

2.2.2. Principles

WEDM is a non-traditional machining process that removes material through a series of controlled electrical discharges between a thin, continuously fed wire electrode (typically brass, zinc-coated brass, or molybdenum, with diameters ranging from 0.1 to 0.3 mm) and the workpiece[77]. Both the workpiece and wire must be electrically conductive. The wire never touches the workpiece; instead, sparks occur in the dielectric fluid (commonly deionized water), generating localized high temperatures (8,000–12,000 °C) that melt and vaporize small amounts of material[78].

The energy released in each spark can be expressed by:

$$E = V \times I \times t_{on}$$

Where:

- V = discharge voltage (V),
- I = discharge current (A),
- t_{on} = pulse-on time (s).

Material removal occurs due to rapid melting and vaporization caused by this localized energy. The dielectric fluid simultaneously cools the surfaces and flushes away debris. Key process parameters influencing performance include pulse-on time, pulse-off time, peak current, wire feed rate, wire tension, flushing pressure, and servo control gap. The material removal rate (MRR) and surface roughness (Ra**)** are typically optimized by balancing these parameters. In WEDM, the wire is continuously renewed, so electrode wear is negligible compared to conventional EDM[78].

2.2.3. Operational Procedure

The WEDM process used in this study was carried out using a high-precision CNC-controlled wire-cut EDM machine. The workflow consisted of the following steps:

- **Workpiece setup:** The platform of Ti-21S samples fabricated by LP-DED was fixed on the machine table and accurately aligned using a dial indicator.
- **Wire selection:** A 20 **µm** titanium wire was employed as the electrode due to its good conductivity, tensile strength, and stable cutting performance. Wire tension and feed rate were adjusted according to the machine manufacturer's guidelines.
- **Parameter setting:** Optimized parameters (pulse on/off times, peak current, servo voltage, and flushing pressure) were programmed to ensure stable discharge conditions. Multiple skim passes were planned to achieve the required surface finish and dimensional accuracy.
- **Cutting operation:** The wire was guided by upper and lower CNC controlled diamond guides, while the programmed toolpath (derived from CAD data) was followed to cut the samples. The continuous movement of the wire and synchronized dielectric flushing ensured removal of molten material and prevention of secondary discharges.

This process enabled precise cutting of Ti-21S samples into the desired dimensions with minimal thermal damage to the bulk material due to the localized nature of the sparks and efficient cooling provided by the dielectric fluid.

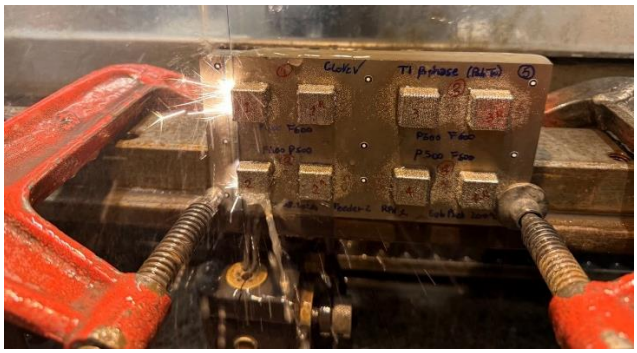

Figure 9. WEDM machine configuration during cutting.

2.3. Samples Characterization

After detachment from the substrate, the fabricated Ti-21S components (Figure 14) were subjected to a comprehensive post-processing characterization program aimed at evaluating their porosity, mechanical performance, and corrosion resistance. The assessment involved a combination of complementary techniques, including optical microscopy for general microstructural observations, scanning electron microscopy (SEM) for detailed morphological and defect analysis, density measurements for quantifying bulk porosity, and high-resolution X-ray computed tomography (CT) scans to identify and visualize internal defects in three dimensions.

Furthermore, nanoindentation and microhardness testing were conducted to investigate the local mechanical response, while uniaxial testing was used to determine the global mechanical properties of the samples[79]. Electrochemical methods, such as potentiodynamic polarization and electrochemical impedance spectroscopy (EIS), were employed to characterize the corrosion behavior in simulated physiological environments. These combined characterization methods provided critical insights into the relationship between the optimized LP-DED processing parameters, resulting microstructure, and the final properties of the Ti-21S alloy. The findings not only validate the effectiveness of the chosen manufacturing strategy but also contribute to guiding future refinement of LP-DED parameters to achieve enhanced performance for biomedical and aerospace applications .[80]

2.3.1. Stereomicroscope

Stereomicroscopy offers low-magnification, three-dimensional visualization of specimens, making it particularly suitable for the preliminary examination of materials. Unlike conventional compound microscopes, stereomicroscopes employ two distinct optical paths that deliver slightly offset images to each eye. This configuration produces a stereoscopic effect, thereby enhancing the perception of depth and allowing for a more accurate assessment of surface topography[81].

In the context of additive manufacturing (AM), this technique plays an important role in the non-destructive evaluation of fabricated components. Stereomicroscopy is especially useful for the initial inspection of external porosities, enabling the identification of defects such as unmelted or partially melted particles, micro-cracks, irregular surface textures, and localized porosity. By incorporating stereomicroscopy into the characterization workflow, potential irregularities in the manufacturing process can be detected at an early stage, supporting process optimization and improving the consistency, efficiency, and reliability of AM parts[82]. Figure 5 illustrates a representative stereomicroscopic image highlighting the surface quality assessment of AM-produced samples.

2.3.2. Density Measurement

The Archimedes method is one of the most widely adopted techniques for measuring the density of additively manufactured components, particularly those produced by Directed Energy Deposition (LP-DED) and other powder-based AM processes. This method is valued for its simplicity, cost-effectiveness, and ability to provide reasonably accurate estimates of bulk density and porosity in metallic parts [180] also, this method is one of the non-destructive tests [85].

The principle of the Archimedes method is based on the classical buoyancy concept formulated by Archimedes, who originally investigated the relationship between volume and displaced fluid. By measuring the weight of a specimen in air and subsequently in a fluid of known density (typically water or ethanol), it is possible to calculate the specimen’s volume from the buoyant force experienced in the liquid [86]. The bulk density (ρ) of the component is then determined using the following relationship:

$$\rho_{Archimedes} = \rho_{liquid} \times \frac{W_{dry}}{W_{dry} - W_{wet}}$$

$$\rho_{Geometrical} = \rho_{liquid} \times \frac{W_{dry}}{W_{dry} - W_{immersion}}$$

$$Total\ Prosity\ Percentage = \frac{\rho_{theorical} - \rho_{bulk}}{\rho_{theorical}} \times 100$$

$$\rho_{Archimedes} = Archimedes\ Density = Apparant\ density\ (\frac{g}{cm^3})$$

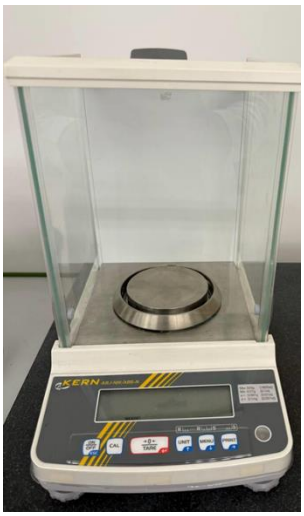

Figure 10. Archimedes balance.

It is important to note that during the weighing of a sample in a fluid, care must be taken to remove all bubbles from its surface, as their presence can significantly affect the measurement results. Similarly, in the final drying step, the same procedures and protocols should be strictly followed to ensure consistency and accuracy of the data. Maintaining uniformity in both the immersion and drying steps is crucial for reproducible results, as any deviation in handling, timing, or environmental conditions could introduce errors. Additionally, documenting each stage of the process and monitoring temperature and humidity during drying can further enhance the reliability of the measurements, particularly when comparing multiple samples or conducting repeated trials. In the upcoming paragraphs, you can see the results in Table 4.

All the Archimedes' tests of Ti21S were done in the standard situation, water as a liquid with 24 celcious and Bulk Density is equal to 4.94 g/cm³.

2.3.3. X-ray computed tomography (CT)

Computed Tomography (CT) is a non-invasive imaging method that generates three-dimensional representations of an object's internal structure. It works by using X-rays in combination with a rotating source-detector system to capture multiple projections, which are then reconstructed mathematically into a 3D image[87]. Compared to conventional radiography, CT provides better contrast, though its spatial resolution is somewhat lower. This technique is widely applied in fields such as medical diagnostics, materials science, engineering, and paleontology [88]. A notable advanced system for CT analysis is the Phoenix v|tome|x s, a high-resolution, versatile platform suitable for both 2D X-ray inspections and 3D computed tomography, including micro-CT and nano-CT imaging. The system is highly adaptable, supporting either a 180 kV/15 W high-power nano-focus X-ray tube or a 240 kV/320 W microfocus tube, which allows it to handle a wide variety of applications. This combination enables the v|tome|x s to deliver extremely high-resolution scans for low-density materials while also permitting 3D analysis of highly absorbing objects [89]. These features make it a powerful and reliable tool for evaluating additive manufacturing (AM) components, identifying unmelted powder areas, voids, cracks, and other structural defects.

Figure 11. Phoenix v|tome|x s CT machine with integrated interface.

2.3.4. Surface Roughness measurement

To characterize the surface texture of the produced components, a profilometer (RTP80-TL90, Someco SM SRL, Italy) was employed to evaluate surface roughness, as illustrated in Figure 18. The device works by moving a high-precision stylus across the surface to detect height variations

and generate a complete map of the surface topography. Key roughness parameters, which serve as indicators of surface quality and manufacturing performance such as Ra[1] , Rz[2] , and Rt[3] can be determined using this approach[90].

For each sample, three measurements were taken at different locations (Left, right and the middle of the sample) to ensure reliability and reproducibility of the data. To account for local variations and minimize measurement uncertainties, the final roughness value for each surface was obtained by averaging the recorded readings. The profilometer was calibrated according to standard surface metrology procedures, with appropriate cut-off lengths and stylus speed settings applied.

Surface roughness measurements, when combined with mechanical testing, offer a thorough understanding of material performance and can guide the optimization of process parameters to enhance surface quality. Furthermore, analyzing the relationship between roughness metrics and functional properties such as mechanical strength, or can provide valuable insights for improving both the durability and the overall performance of the components. Such comprehensive evaluation ensures that manufacturing processes are refined to achieve consistent, high-quality surfaces across all produced parts. You can see the results of Surface Roughness measurement in Figure 13 and Table 5.

Figure 12. Profilometer RTP80-TL90.

2.3.5. X-ray diffraction

The phase composition of the samples was analyzed using X-ray diffraction (XRD) with a The Bruker device was used with Cu Kα radiation (λ = 1.5406 Å) at a tube voltage of 50 kV and a current of 30 mA. The investigated 2θ range was from 5° to 100°. The measurements were performed on polished specimens to ensure accurate and representative results. XRD allows for the identification of crystalline phases and provides information on the material's structural characteristics, including lattice parameters and possible phase transformations. For enhanced reliability, the diffraction patterns were collected over a wide range of angles with fine step sizes, enabling precise detection of minor phases . The obtained data were subsequently compared with standard diffraction databases to confirm phase identification. In addition, quantitative phase analysis can be conducted using Rietveld refinement or similar methods, offering insights into the

[1] arithmetical mean roughness
[2] maximum profile height
[3] total height variation

relative proportions of different phases. Understanding the phase constitution is crucial for correlating microstructural features with mechanical properties, thermal stability, and overall material performance, thereby guiding optimization of processing parameters for improved material quality[91].

2.3.5.1. Phase Constitution and Texture

The X-ray diffraction (XRD) patterns of the powder and the four as-built samples are presented in diagram 3 All diffraction patterns display peaks corresponding exclusively to the β-phase, indicating that the material retains a single metastable β-phase both in powder form and after additive manufacturing. No peaks related to α or α'-martensite phases were observed, confirming the absence of these phases in the processed samples. The primary reflections of the β-phase are located at 2θ values of approximately 38°, 55°, 70°, 77°, and 93°, corresponding to the (110), (200), (211), (220), and (310) crystallographic planes, respectively. When comparing the powder with the as-built samples, a noticeable change in the relative intensity of the diffraction peaks can be observed. This variation indicates the development of a crystallographic texture during the additive manufacturing process. In particular, the (110) peak exhibits the highest intensity in all as-built samples, suggesting a preferred orientation along this plane. Such texturing is commonly observed in additively manufactured β-titanium alloys and can influence mechanical properties by introducing anisotropy in the material's microstructure [92].

To further validate these observations, XRD measurements were conducted on samples with different orientations, confirming the consistency of the β-phase across all examined directions. The comparison of diffraction patterns among Sample 1 through Sample 4 shows minor variations in peak intensities, which may be attributed to local differences in cooling rates or build orientations during the fabrication process. Overall, the XRD results demonstrate that the additive manufacturing process preserves the metastable β-phase while inducing a mild crystallographic texture, providing insights into the structural characteristics and expected mechanical behavior of the material [93].

2.3.6. Microstructure analysis

2.3.6.1. Metallography

2.3.6.1.1. Grinding

Manual surface grinding was performed using the Presi Minitech 250/300 SP1 grinding machine (Figure 13), with continuous water flow applied to avoid overheating and to prevent contamination of the material, as illustrated in Figure 14. A sequence of silicon carbide abrasive papers with grit sizes of 600, 800, 1200, and 2400 was employed to progressively smooth the surface, ensuring uniformity in preparation for subsequent polishing and etching procedures.

Following the grinding process, the specimens were polished using progressively finer polishing compounds to remove any micro-scratches left by the abrasive papers. This step ensured a mirror-like surface finish, which is critical for accurate metallographic examination. Once the desired surface quality was achieved, the samples underwent chemical etching using an appropriate etchant to reveal the underlying microstructure. The etched surfaces were then examined under an

optical microscope to evaluate the material's grain structure, phase distribution, and any surface defects introduced during processing [94].

Figure 13. Presi Mini tech 250/300 SP1 grinding machine.

After each stage, the specimens were examined under a microscope to assess the surface quality. If any grinding marks were still visible, the sample was rotated by 90° and polished with a finer grit abrasive to eliminate them. Once the grinding lines were completely removed, the polishing process was carried out to further refine the surface and eliminate any remaining micro-scratches.

2.3.6.1.2. Polishing

Polishing of the ground specimens was carried out using silica liquid as a lubricant to achieve a smooth, defect-free surface. Initially, a 3µm aluminum oxide mixed with a small amount of water was applied to remove the deeper scratches and marks left from the previous grinding stages. The polishing process was performed carefully to ensure uniform material removal and to avoid introducing new surface irregularities.

Polishing was carried out using pads with 3 µm and 1 µm diamond suspensions in succession, followed by a final polish with a 0.3 µm aluminum oxide solution to produce a smooth, mirror-like surface. This multi-step polishing procedure ensured the complete removal of scratches and surface irregularities from the previous grinding and polishing stages.

Once the desired surface quality was achieved, the prepared samples were subjected to chemical etching to reveal the underlying microstructure. The etching process highlighted the grain boundaries, phases, and other structural features, enabling detailed examination under an optical microscope. This step was crucial for assessing the material's characteristics, identifying any defects, and preparing the samples for subsequent metallographic analysis [95].

2.3.6.1.3. Etching

During the etching process, the interaction between the Krool etchant and the sample surface accentuated the microstructural details, making grain boundaries, phases, and any defects clearly visible. The samples were closely monitored to ensure uniform etching across the surface, preventing uneven attacks that could obscure important features. After etching, the specimens were thoroughly rinsed with water and gently dried to stop the chemical reaction and preserve the revealed microstructure. The resulting surfaces, which are shown in the images below, provided a clear and accurate representation of the material's microstructure, enabling detailed examination and analysis under an optical microscope [96].

Figure 14. Etching process of the samples with Kroll etchant.

2.3.6.2. Optical Microscopy (OM)

After completing the metallography preparation and etching steps, the samples were examined using an optical microscope Lacia DM6. This instrument was employed to capture high-quality images of the microstructure at different magnifications, enabling detailed observation of the grain boundaries, phases, and other microstructural features revealed by the etching process [97].

Micrographs were taken at 5×, 10×, and 20× magnifications, providing a comparative view of the surface at different scales. The lower magnification allowed for an overall assessment of the general microstructural distribution, while the higher magnifications offered precise visualization of finer details and features not visible at lower resolutions. This multi-scale approach ensured accurate documentation and reliable analysis of the material's microstructure [98].

2.3.7. Mechanical Properties

2.3.7.1. Micro Vickers

The mechanical properties of the prepared samples were first evaluated using the Micro Vickers hardness test. This technique is widely employed for characterizing small-scale materials and thin sections due to its high precision and ability to measure localized hardness. The method is based on applying a controlled load through a diamond indenter with a pyramidal geometry (square base and an angle of 136° between opposite faces) onto the polished surface of the sample. After the load is applied and removed, the resulting indentation is measured under a microscope, and the

hardness value is calculated from the applied load divided by the surface area of the indentation [99].

Figure 15. Micro Vickers machine.

Figure 16. Impact of diamond indenter on the surface of the sample.

The Micro Vickers test is particularly suitable for metallographic samples, as it allows for assessing hardness at microstructural levels without causing significant damage to the specimen. By using relatively low loads, the technique makes it possible to evaluate hardness variations

within different regions of the material, providing valuable information about the correlation between microstructure and mechanical behavior. This precision makes the test highly effective for understanding phase distribution, grain boundaries, and localized strengthening mechanisms within the analyzed alloys.

For each sample, five individual measurements were performed at different positions on the polished and etched surface to ensure repeatability and reduce statistical error. The average of these values was then reported as the representative hardness of each sample. This approach minimizes local variations and provides a reliable basis for comparing mechanical properties across different samples and processing conditions.

2.3.7.2. Nano Indentation

In order to evaluate the local mechanical response of the specimens beneath the surface following the applied treatments, nanoindentation experiments were conducted using a Hysitron TI 950 TriboIndenter® (Bruker Nano Surfaces, USA)**,** as illustrated in Figure 20. This state-of-the-art equipment operates with capacitive transducer technology in combination with a Performech® Advanced Control Module, which ensures exceptional sensitivity and minimal signal noise. The system provides force and displacement resolutions better than 2 nN and 0.02 nm, respectively. Such advanced precision makes the instrument highly suitable for accurate mechanical characterization across a wide range of materials, from hard coatings to softer systems. In particular, it is extensively used for metallic alloys such as titanium-based materials, where sub-surface property evaluation is crucial for understanding the effects of processing and surface modification [100].

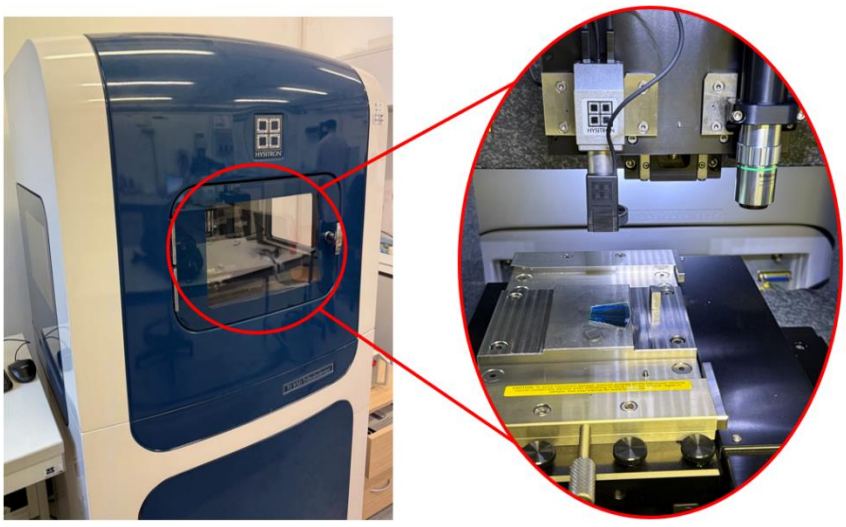

Figure 17. Hysitron TI 950 TriboIndenter® (Bruker Nano Surfaces, USA).

The specimens were prepared in advance and, due to their appropriate dimensions, they were not mounted. Their rigidity and stability made them suitable for direct testing. The surfaces underwent successive polishing steps down to a final finish of 0.03 μm, after which they were carefully cleaned and dried to ensure the removal of any residual contaminants.

For the nanoindentation experiments, a Berkovich diamond indenter with a three-sided pyramidal geometry was used (Figure 21). The corresponding loading–unloading curve is presented in Figure 22. Indentations were arranged in a grid pattern, with nine repetitions for each testing condition, ensuring statistical reliability. To minimize interactions between adjacent indents, the spacing between them was maintained at no less than 20 μm, preventing overlap of the plastic deformation zones.

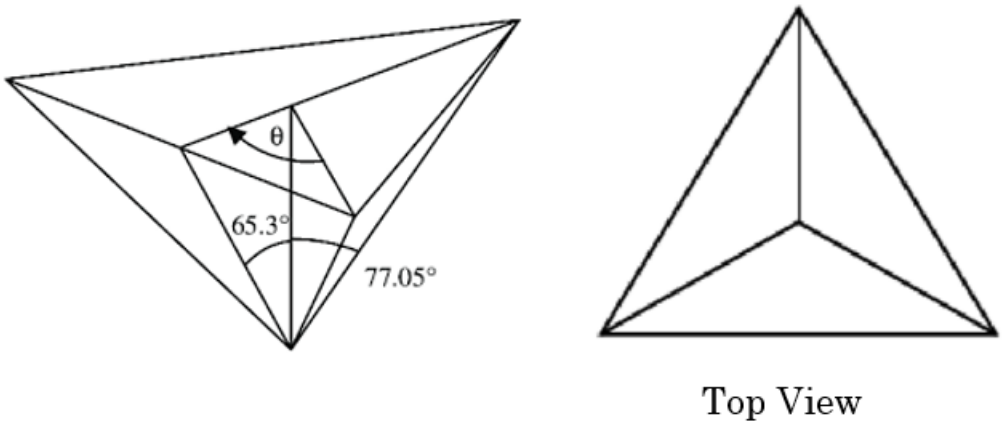

Figure 18. Schematic of a Berkovich indenter tip

The hardness (H) and reduced elastic modulus (Er) were derived from the load-displacement curves using the Oliver-Pharr method [101]:

$$H = \frac{P_{max}}{A_C}$$

$$E_r = (\frac{\sqrt{\pi}}{2\beta}) \times (\frac{S}{\sqrt{Ac}})$$

where:

• P_{max} = Maximum applied load (mN)

• Ac = Projected contact area (nm²), calculated via the tip area function

• S = Contact stiffness (mN/nm), extracted from the unloading curve slope

• β = Geometric correction factor (~1.034 for Berkovich tip)

The elastic modulus of the sample (E_s) was calculated from E_r by accounting for the indenter's modulus (E_i = 1141 GPa for diamond) and Poisson's ratio (ν_i = 0.07), assuming a sample Poisson's ratio (ν_s) of [0.3 for metals]:

$$\frac{1}{E_r} = (1 - \nu_s^2)/E_s + (1 - \nu_i^2)/E_i$$

Nanoindentation-derived hardness and modulus values were used to estimate wear resistance through the H/E_r ratio (elastic strain to failure) and H^3/E_r^2 (resistance to plastic deformation) [189]:

Wear resistance indicators:

$$\frac{H}{E_r} \ \& \ \frac{H^3}{E_r^2}$$

Higher H/E_r ratios (>0.1) suggest improved elasticity and crack resistance, while elevated H^3/E_r^2 values correlate with enhanced resistance to abrasive wear.

2.3.8. Corrosion Resistance

The mechanical performance of metallic implants measured under ambient conditions can be significantly altered by environmental influences. Although the human body provides a relatively stable environment, variations in temperature, chemical composition, or pH levels often associated with pathological conditions such as inflammation or allergic reactions can impact implant behavior. Long-term exposure of implant surfaces to corrosive environments may cause gradual degradation, eventually compromising structural integrity. Titanium and its alloys are widely used in biomedical applications because of their ability to form a protective passive oxide layer, primarily composed of TiO_2. This layer is self-healing, meaning it can readily reform when scratched or disrupted, which plays a critical role in maintaining the predicted mechanical properties of implants and preventing premature failure [102]. Extensive research has examined the corrosion resistance of commercially pure titanium (CP-Ti), Ti-6Al-4V, and β-Ti alloys.

Figure 19. Electrochemical process.

This work studied the corrosion behavior of the AM Ti–6Al–4V alloy and observed that the difference between the corrosion rates of the planes parallel and perpendicular to the substrate can be attributed to the formation of a "weaker" passive layer on the planes and the higher portion of acicular martensitic α′ phase along the planes perpendicular to the substrate.[103]. The corrosion resistance of the AM Ti–6Al–4V alloy is affected by the types of ions present in the aqueous solutions. Halide solutions, especially those containing Cl^- or Br^- ions, may play an important role with respect to the reduction of the localized corrosion resistance of the AM Ti alloys. [104]. Similar investigations on β-Ti alloys have shown superior corrosion resistance compared with CP-Ti and α+β alloys. For instance, compared CP-Ti, Ti-6Al-4V, and Ti-24Nb-4Zr-8Sn in simulated physiological conditions and demonstrated that the β-Ti alloy exhibited a broader passive range and lower corrosion current density, attributed to the stability of the oxide film enriched with titanium and niobium oxides. Likewise reported that Ti-Zr-Nb-Mo alloys containing 15 wt.% Mo showed the lowest passivation current density (2.31 ± 0.03 μA cm^{-2}). examined Ti-15Mo, CP-Ti, and Ti-6Al-4V in Ringer's solution and concluded that all tested alloys were resistant to corrosion, with Ti-15Mo forming a particularly stable passive film, making it promising for biomedical applications [105].

Overall, β-type titanium alloys consistently demonstrate superior corrosion resistance compared with CP-Ti and α+β alloys. However, it is essential to consider the potential formation of secondary or parasitic phases during thermal treatments, as these can significantly deteriorate corrosion performance and compromise long-term implant reliability.

The advantages of β Ti alloy involve their excellent biocompatibility, high strength, good corrosion resistance, and the better manufacturability compared the other high performance alloys (Kolli and Devaraj 2018). In some β-Ti alloys superelasticity is an important property for some biomedical applications i.e., the stent [106].

3. Results and Discussion

3.1. Sumup

This section provides a detailed evaluation of the influence of Directed Energy Deposition (DED) process parameters on the density, microstructure, corrosion resistance, and mechanical properties of Ti-21S alloy components. The analysis begins with the process optimization stage, where relative density was quantified using both tomography and Archimedes' methods, complemented by preliminary mechanical property assessments.

The role of process parameters in controlling density and surface roughness was systematically investigated to establish a set of optimized fabrication conditions. SEM micrographs and surface profilometry were employed to characterize the resulting microstructural features and topographical variations. The roughness profiles, in particular, revealed the correlation between process settings and surface quality, offering insight into the underlying mechanisms governing defect formation and layer bonding.

3.2. Density results

The density of the deposited material is strongly governed by the applied Linear Energy Density (LED), which itself is determined by the interplay between laser power, scanning speed, and hatch distance. In this study, the hatch distance was fixed at 50 μm, while laser power and scanning speed were systematically varied, as summarized in Table 7. The average densities measured using the Archimedes' method are presented in Table 4. These values ranged between 4.92 g/cm³ and 4.93 g/cm³, corresponding to relative densities of approximately 99.6%–99.9% when compared to the theoretical density of Ti-21S (4.94 g/cm³). Such high values indicate that the selected parameter window was effective in minimizing porosity and promoting near-full densification of the alloy.

Table 5. Table 8. Results of Archimedes' test.

Sample N.1	**Dry Weight**	**Wet Weight**	**Humid Weight**	**Density**	**Percentage**	**STDEV**	**Average**
Test 1	7.6857	6.1319	7.6861	4.9315	99.80	0.1026	99.8733
Test 2	7.6858	6.1333	7.6859	4.9357	99.90		
Test 3	7.6858	6.1335	7.6859	4.9363	99.92		
Sample N.2	**Dry Weight**	**Wet Weight**	**Humid Weight**	**Density**	**Percentage**	**STDEV**	**Average**
Test 1	6.8784	5.4860	7.8786	4.9251	99.69	0.152	99.6933
Test 2	6.8784	5.4862	7.8784	4.9350	99.71		
Test 3	6.8784	5.4858	7.8788	4.9244	99.68		
Sample N.3	**Dry Weight**	**Wet Weight**	**Humid Weight**	**Density**	**Percentage**	**STDEV**	**Average**
Test 1	7.6326	6.0867	7.6327	4.9225	99.63	0.1026	99.7433
Test 2	7.6325	6.0897	7.6327	4.9323	99.83		
Test 3	7.6324	6.0890	7.6328	4.9290	99.77		
Sample N.4	**Dry Weight**	**Wet Weight**	**Humid Weight**	**Density**	**Percentage**	**STDEV**	**Average**
Test 1	7.1072	5.6719	7.1074	4.9368	99.92	0.0513	99.9066
Test 2	7.1071	5.6708	7.1072	4.9330	99.85		
Test 3	7.1073	5.6722	7.1073	4.9376	99.95		

The marginal variations in relative density suggest that small fluctuations in LED can influence the degree of pore elimination and melt pool stability. At higher energy densities, more complete melting occurred, reducing the likelihood of lack-of-fusion defects. However, excessive energy input may also promote keyhole porosity or evaporation-related defects, highlighting the importance of balancing the process window. The consistency of density values across the tested parameters confirms the robustness of the chosen strategy and provides a reliable foundation for subsequent mechanical and microstructural characterization.

To further validate these findings, density was also assessed by X-ray tomography. The results corroborated Archimedes' measurements, revealing a low defect volume fraction and confirming that pores, when present, were typically spherical and uniformly distributed. This observation indicates that the process settings successfully suppressed critical defect types such as elongated lack-of-fusion pores, which are known to compromise fatigue performance. In the following sections, the influence of these optimized process conditions on surface morphology, microstructure, and mechanical behavior is discussed in greater detail, establishing the direct link between densification, microstructural integrity, and the overall performance of Ti-21S alloy components.

X-ray computed tomography (XCT) was employed to quantify the morphology and spatial distribution of internal porosity within the fabricated samples. As illustrated in Figure 28, specimens processed at lower energy densities exhibited irregular and elongated pores, a feature typically associated with incomplete fusion between adjacent layers. In contrast, samples produced under higher energy densities contained smaller, more spherical pores, which are generally attributed to keyholing or the entrapment of shielding gas within the melt pool.

The overall porosity fraction across all conditions ranged between 0.2% and 0.5%, with the lowest values recorded in samples 1, 3, and 4 corresponding to those with the highest measured densities. Importantly, no evidence of significant pore clustering was detected, suggesting uniform powder spreading and stable energy input throughout the build process.

These findings highlight the delicate balance between insufficient and excessive energy input. While lower energy densities increase the risk of lack-of-fusion defects, overly high energy input may induce keyhole-related porosity. The relatively low porosity levels achieved across the tested conditions reinforce the effectiveness of the optimized parameter set and are expected to contribute positively to the mechanical reliability of Ti-21S components. In the subsequent section, the relationship between porosity features and surface roughness will be examined to further elucidate their combined effect on the mechanical performance and corrosion resistance of the alloy.

3.3. Surface roughness measurement and Stereo Microscopie

Surface roughness was assessed using contact profilometry, with arithmetic average roughness (Ra) values ranging from 8 µm to 18 µm, as presented in Table 5. Typically, higher scan speeds combined with lower energy densities are associated with increased roughness, primarily due to the presence of partially melted particles and the occurrence of balling along the scan tracks. In the present work, however, the applied process window was relatively narrow, which limited the

ability to establish strong correlations between specific process parameters and the resulting surface quality.

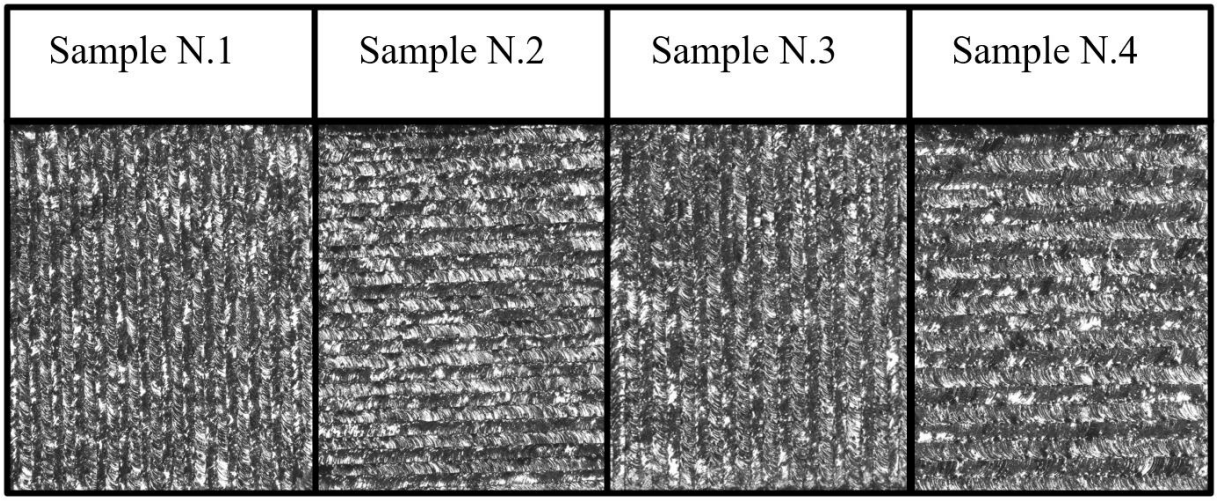

Figure 20. stereomicroscope image of upper surface of samples.

Beyond surface inspection, stereomicroscopy also assists in the preparation of specimens for more advanced characterization techniques. By providing a broad field of view, it allows researchers to precisely locate areas of interest prior to sectioning or further high-resolution analyses such as scanning electron microscopy (SEM) and computed tomography (CT) [83]. As a result, stereomicroscopy serves as a complementary tool within the multi-scale characterization pipeline of AM components, bridging the gap between macroscopic and microscopic observations [84]. Its rapid, accessible, and cost-effective nature makes it indispensable for quality control and research in both laboratory and industrial settings.

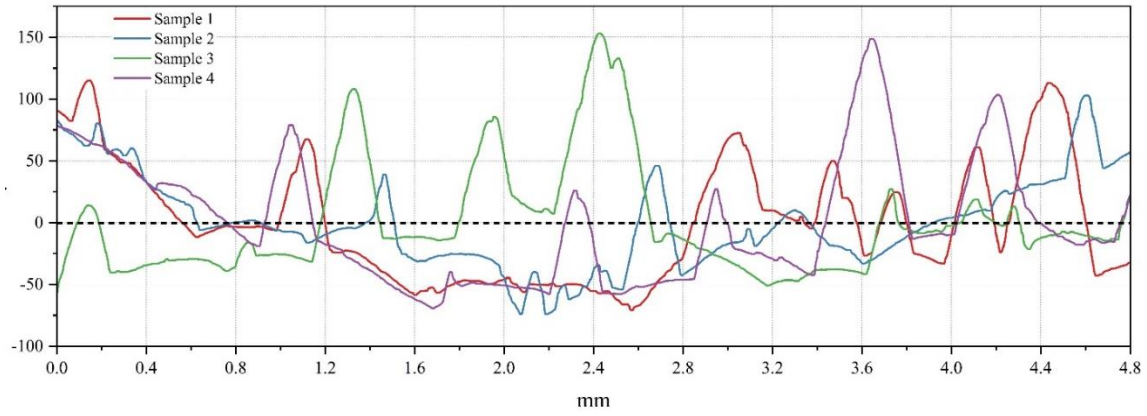

Diagram 1: Diagram of roughness measurement of samples

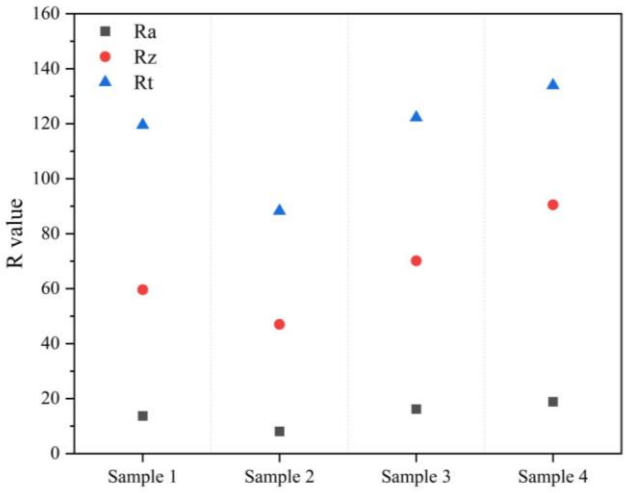

Diagram 2: Comparison between the results of the roughness measurement of the samples.

Table 6. Results of roughness measurement of samples.

	Sample N.1	**Sample N.2**	**Sample N.3**	**Sample N.4**
Ra	13.725 µm	8.128 µm	16.219 µm	18.864 µm
Rz	59.654 µm	46.993 µm	70.128 µm	90.546 µm
Rt	119.548 µm	88.276 µm	122.258 µm	133.96 µm

It is worth noting that the surface state plays a decisive role not only in fatigue performance but also in corrosion behavior. Rougher surfaces tend to promote localized corrosion initiation by providing crevice-like sites and retaining residual stress. Thus, surface finishing serves a dual purpose ensuring dimensional accuracy and improving both mechanical and electrochemical performance.

Nevertheless, Ra values below 10 µm were achieved under certain conditions, which can be regarded as acceptable in terms of reducing the extent of post-processing required. Despite this, post-fabrication surface finishing remains indispensable to meet the strict quality and durability standards expected of high-performance Ti-21S components. Such treatments not only further reduce surface roughness but also eliminate loosely bonded particles and enhance fatigue resistance, particularly in applications where cyclic loading and long-term reliability are critical.

3.4. Mechanical Results

In the following section, these observations are correlated with microstructural analysis to better understand how process-induced features, including porosity and surface morphology, collectively influence the mechanical response of Ti-21S alloy components. To evaluate the mechanical response of the Ti-21S alloy, nanoindentation and micro-Vickers measurements were employed to determine hardness (H) and reduced modulus (Er). The obtained results were consistent with the trends observed in the load–displacement curves, as shown in Figure NN. Notably, the as-built,

ground, and chemically polished specimens exhibited comparable hardness values, indicating that surface finishing had only a marginal influence on the bulk hardness of the material.

Table 7. Results of micro-Vickers.

Sample Number	HV	STDE
Sample N.1	357	24.4741
Sample N.2	378	12.5982
Sample N.3	332	19.3647
Sample N.4	388	15.4299

This similarity suggests that the primary strengthening mechanisms are governed by the intrinsic microstructure formed during the additive manufacturing process rather than surface state modifications. While grinding and chemical polishing were effective in reducing surface roughness, their effect on subsurface mechanical properties was minimal, as hardness is largely dictated by grain morphology, phase distribution, and residual stresses within the bulk material.

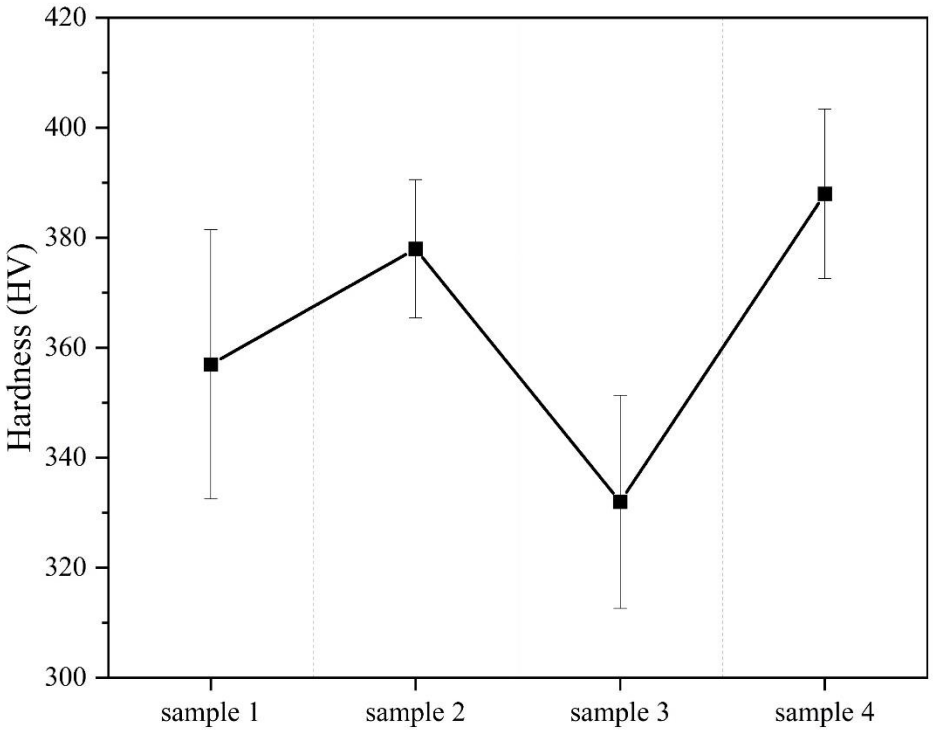

Diagram 3: Comparison of the micro-Vickers results.

The reduced modulus (Er) followed similar trends across the different surface conditions, further confirming the stability of elastic behavior regardless of post-processing treatment. These findings imply that surface finishing primarily enhances surface integrity and fatigue resistance, without significantly altering the underlying hardness or stiffness of the alloy.

Furthermore, subsurface mechanical behavior was probed using nanoindentation and micro-Vickers testing. These methods provided valuable information on hardness, elastic modulus, and wear resistance indicators (H/Er and H^3/Er^2), enabling a more comprehensive understanding of how localized microstructural variations affect overall component performance. Collectively, these results highlight the strong interplay between process design, density, and surface finishing in determining the final mechanical response of additively manufactured Ti-21S components.

3.5. Microstructure results

For the final stage of the metallographic preparation, the polished samples were subjected to chemical etching to reveal their microstructure. The Kroll etchant was chosen for this purpose due to its ability to clearly highlight the grain boundaries and structural features of the material. The polished specimens were carefully immersed in the etchant for controlled durations ranging between 8 and 13minutes, allowing sufficient reaction to reveal the microstructure without over-etching.

To analyze the microstructure of the samples, the study began with metallographic preparation. Since the manufacturing process was carried out using Directed Energy Deposition (DED), the melt pools were clearly visible prior to etching figure 21. After etching, a more detailed observation was performed, and images were captured using an Optical Microscope (OM). To further validate the microstructural findings, X-Ray Diffraction (XRD) analysis was conducted. The results confirmed the presence of a fully beta phase structure.

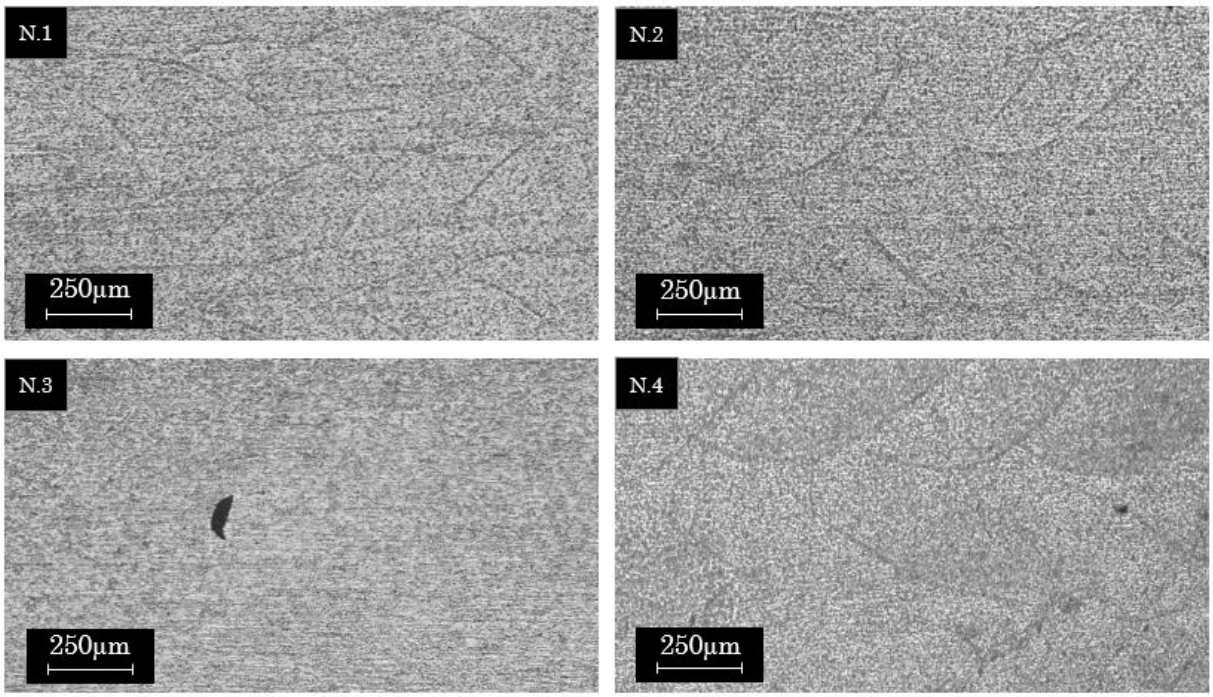

Figure 21. OM images of samples before the etching process.

These observations are consistent with the expected microstructure of alloys produced under rapid solidification conditions, typical of additive manufacturing processes such as DED. The formation of a fully beta phase suggests that the processing parameters were effective in stabilizing the beta structure across the sample. This outcome is particularly significant, as it ensures homogeneity and provides a reliable basis for further mechanical characterization.

Subsequent investigations will focus on correlating the obtained microstructural features with the mechanical properties of the material. Hardness measurements, tensile tests, and fracture analysis will be performed to evaluate the influence of the fully beta phase on the overall performance of the alloy. In addition, scanning electron microscopy (SEM) will be employed to examine the finer microstructural details, such as grain boundaries and potential defects introduced during the DED process.

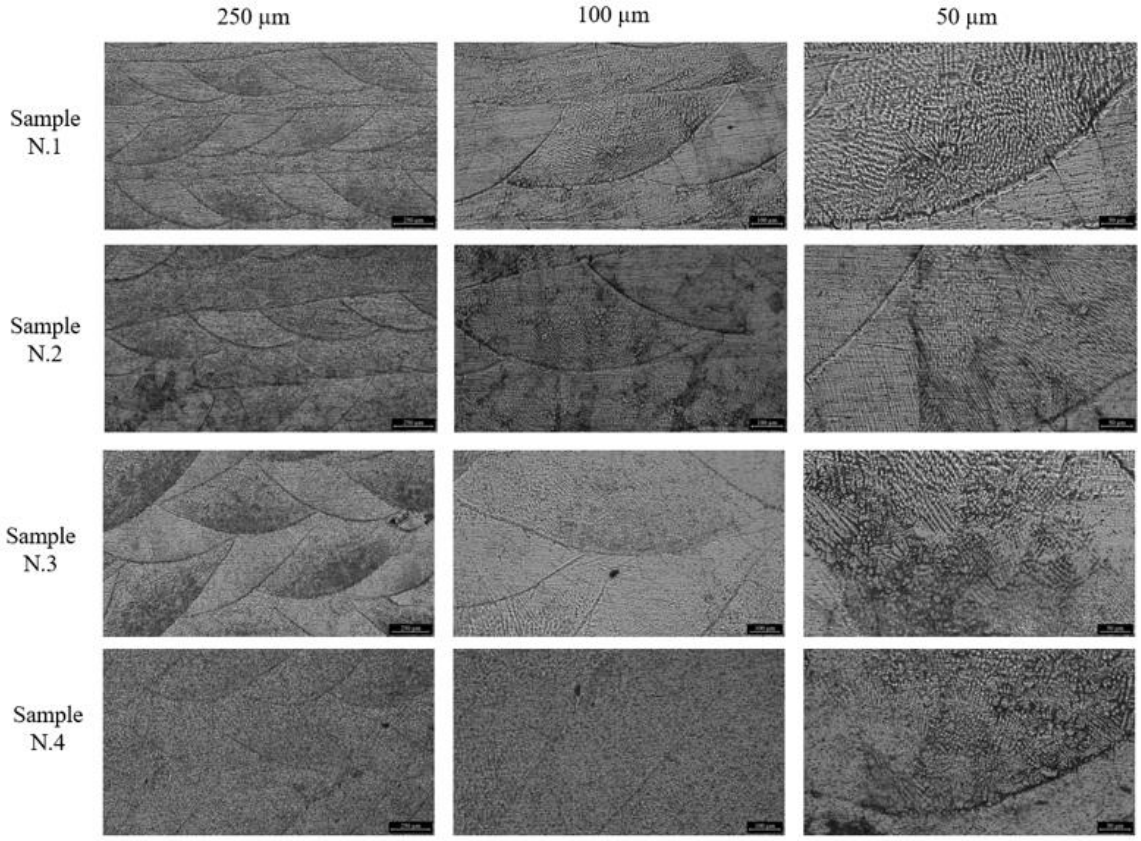

Figure 22. OM images with different resolution after etching process.

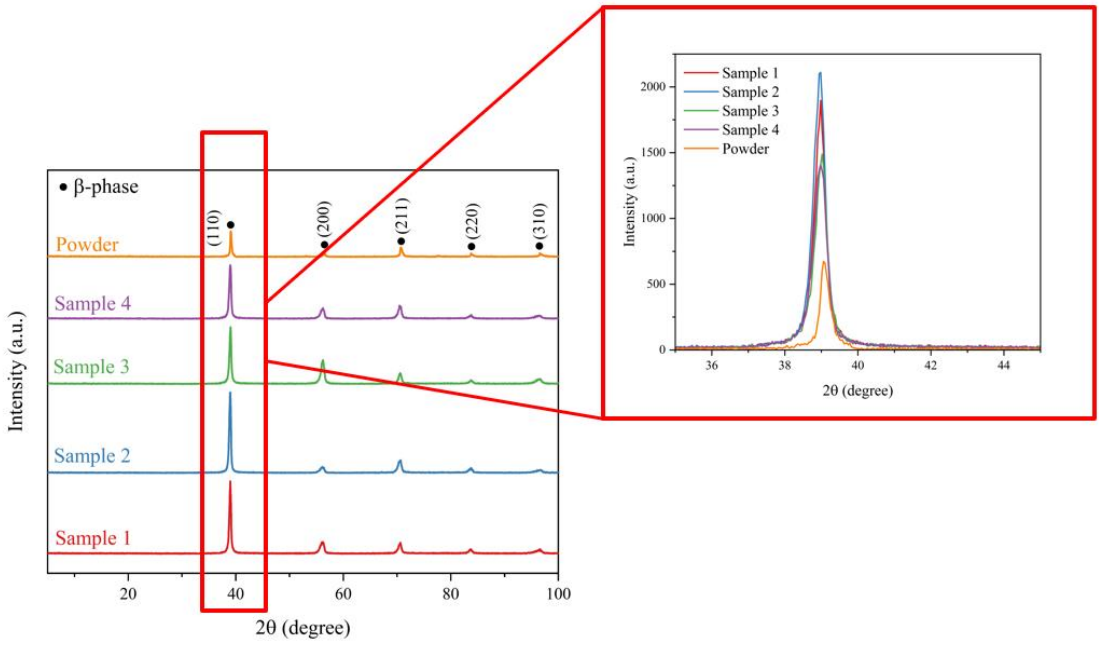

Diagram 4: XRD analysis of samples.

3.6. Corrosion Results

In addition, corrosion resistance was evaluated through electrochemical testing, which confirmed the sensitivity of this novel alloy to both microstructural heterogeneity and surface state. The findings suggest that optimized process parameters not only enhance mechanical reliability but also contribute to improved corrosion resistance, thereby extending the potential service life of Ti-21S in demanding environments.

Following fabrication, the specimens were subjected to surface preparation: sequential wet grinding using 2400-grit SiC paper, polishing with a 1 μm alumina suspension, rinsing with double-distilled water, and finally air drying. Prior to electrochemical evaluation, aqueous electrolyte solutions of 0.9 % NaCl . These electrolytes were used to assess the corrosion performance of the fabricated alloys under simulated aggressive environments.

Electrochemical corrosion testing further highlighted the promise of this alloy. When compared to Ti-6Al-4V, Ti-21S demonstrated comparable, and in some cases superior, resistance to corrosive attack. This enhanced performance can be attributed to the alloy's refined microstructure and stable passive film formation, both of which are strongly influenced by the optimized LP-DED process. The corrosion behavior, combined with the mechanical properties that closely approximate those of human cortical bone, positions Ti-21S as a particularly attractive candidate for biomedical applications in addition to aerospace components, where both durability and biocompatibility are essential.

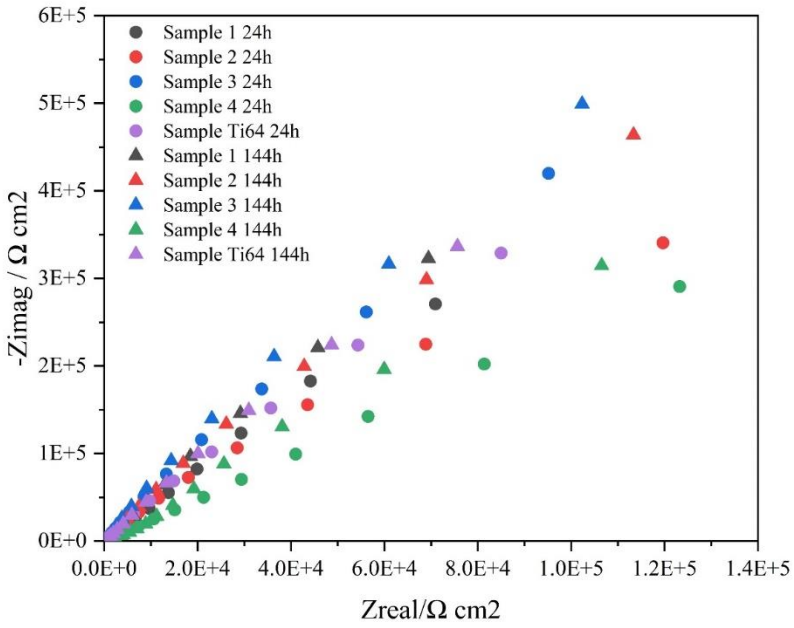

Diagram 5: Nyquist and Bode plots of samples at various times.

In this study, additively manufactured (AM) Ti 64 and Ti–21S alloys were investigated. Rectangular samples with dimensions of 20 × 20 × 12 mm³ were fabricated using the Directed Energy Deposition (DED) process (Subsii, Switzerland). The deposition was carried out under an argon (Ar) protective atmosphere, with a laser power of 500–600 W and a scanning speed of 500 mm/min. The feedstock powders were co-injected during deposition, and their nominal composition (in wt.%) was: C: 0.011, Fe: 0.18, Al: 6.1, V: 3.7, Sn: 0.01, Ti: balance.

Additionally, derived wear resistance indicators, such as H/Er and H^3/Er^2, were calculated to provide deeper insight into the balance between hardness and modulus. These ratios revealed that the alloy possesses a favorable combination of strength and resistance to plastic deformation, particularly under the optimized processing conditions. This highlights the potential of Ti-21S for applications requiring high durability under mechanical loading.

In the subsequent discussion, these results are correlated with microstructural observations and porosity measurements to establish the links between processing parameters, microstructural evolution, and mechanical performance. This integrated approach offers a comprehensive understanding of how additive manufacturing strategies can be tailored to unlock the full potential of Ti-21S alloy.

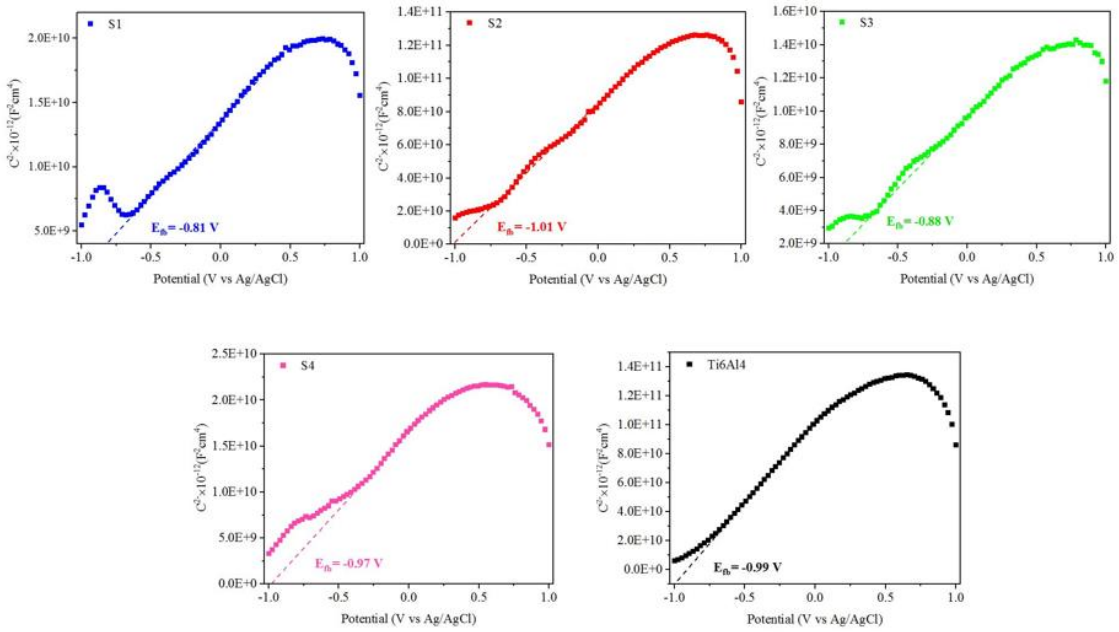

Diagram 6: Mott–Schottky plots of the specimens in 0.9 %wt NaCl solution

Table 8. Electrochemical data of the specimens in 0.9 %wt NaCl solution for various durations, calculated from the circuit models.

Sample	Time (h)	R_{ct} (kΩ)
Sample N.1	24	5.96×10^9
	144	6.52×10^9
Sample N.2	24	6.86×10^9
	144	1.06×10^{10}
Sample N.3	24	8.40×10^9
	144	1.11×10^{10}
Sample N.4	24	6.37×10^9
	144	6.77×10^9
Sample Ti64	24	6.16×10^9
	144	6.61×10^9

Electrochemical Impedance Spectroscopy (EIS) was carried out to evaluate the corrosion behavior of the investigated alloys in 0.9 wt.% NaCl solution, simulating physiological saline conditions. The obtained Nyquist and Bode plots were analyzed using an equivalent Randles circuit model, which consisted of three key elements: solution resistance (Rs), charge transfer resistance (Rct), and a constant phase element (CPEdl) representing the double-layer capacitance. The inclusion of the CPE was necessary to account for deviations from the behavior of an ideal capacitor, which typically arise from surface inhomogeneities, roughness, and localized adsorption phenomena on the alloy surface. As proposed by Brug et al., a mathematical relationship was applied to relate the non-ideal CPE parameters to the effective interfacial capacitance, thereby allowing for a more accurate interpretation of the electrochemical interface.

The EIS fitting results indicated distinct differences between Ti–6Al–4V and Ti–21S. The Ti–21S alloy exhibited higher charge transfer resistance (Rct) compared to Ti–6Al–4V, suggesting a superior ability to resist charge transfer processes and, consequently, a more protective passive film. In contrast, the lower Rct values observed for Ti–6Al–4V reflected a relatively less stable passive layer, more prone to localized breakdown. The phase angle values from Bode plots further confirmed these trends, where Ti–21S displayed a broader capacitive region, indicative of improved electrochemical stability.

Overall, the EIS analysis highlights the enhanced corrosion resistance of Ti–21S alloy in chloride-containing environments, primarily attributed to its refined microstructure and the stable passive oxide layer formed during the DED process.

4. Conclusion and Future Perspectives

This study has provided a comprehensive investigation into the effects of process parameter optimization on the density, mechanical properties, and corrosion resistance of Ti-21S alloy components fabricated via Laser Powder Directed Energy Deposition (LP-DED). By applying a design of experiments (DOE) approach, laser power and scanning speed were systematically varied to establish the most effective combinations of process parameters. Among the four parameter sets examined, sample 4 [P = 500 W; V = 500 mm/s; LED = 1.65 J/mm^3], corresponding to moderate energy input conditions, yielded the highest relative density at 99.9%, demonstrating the robustness of the optimized processing window.

Mechanical characterization using nanoindentation and micro-Vickers testing provided valuable insight into the near-surface response of the alloy. The results indicated consistent hardness and elastic modulus values across different surface conditions (as-built, ground, and chemically polished), suggesting that the bulk mechanical integrity is predominantly governed by the intrinsic microstructure formed during deposition. Importantly, derived wear resistance indices (H/Er and H^3/Er^2) confirmed that Ti-21S exhibits a favorable balance between strength and resistance to plastic deformation, underscoring its potential for use in components subjected to cyclic or contact loading in service.

Overall, this work demonstrates that the simultaneous optimization of LP-DED process parameters and surface condition provides a reliable pathway for producing Ti-21S components with near-full densification, robust mechanical performance, and tailored corrosion resistance. These findings strengthen the case for Ti-21S as a next-generation β-titanium alloy suitable for demanding structural applications.

Future research should expand upon these findings by:

- Conducting advanced microstructural characterization (e.g., EBSD, TEM) to clarify the role of grain refinement and phase transformations on the mechanical response.

- Performing fatigue and tensile testing to establish the long-term reliability of Ti-21S under operational loading conditions.
- Exploring hybrid surface treatment strategies, combining mechanical, chemical, or thermal post-processing to further enhance both mechanical and corrosion performance.
- Investigating process scalability and industrial integration to assess the economic feasibility of deploying optimized LP-DED Ti-21S components at scale in aerospace and biomedical industries.

In conclusion, the integration of process design, mechanical evaluation through nanoindentation and micro-Vickers testing, and corrosion resistance assessment demonstrates that Ti-21S, when fabricated via optimized LP-DED, possesses the key attributes required for qualification in aerospace-grade and high-performance biomedical applications.

5. References

[1] T. Barbin *et al.*, "3D metal printing in dentistry: An in vitro biomechanical comparative study of two additive manufacturing technologies for full-arch implant-supported prostheses," *J Mech Behav Biomed Mater*, vol. 108, Aug. 2020, doi: 10.1016/j.jmbbm.2020.103821.

[2] J. A. Tamayo, M. Riascos, C. A. Vargas, and L. M. Baena, "Additive manufacturing of Ti6Al4V alloy via electron beam melting for the development of implants for the biomedical industry," May 01, 2021, *Elsevier Ltd*. doi: 10.1016/j.heliyon.2021.e06892.

[3] P. Wang, J. Song, M. L. S. Nai, and J. Wei, "Experimental analysis of additively manufactured component and design guidelines for lightweight structures: A case study using electron beam melting," *Addit Manuf*, vol. 33, May 2020, doi: 10.1016/j.addma.2020.101088.

[4] M. Srivastava *et al.*, "Additive manufacturing of Titanium alloy for aerospace applications: Insights into the process, microstructure, and mechanical properties," Dec. 01, 2024, *Elsevier Ltd*. doi: 10.1016/j.apmt.2024.102481.

[5] A. Arjunan, A. Baroutaji, and A. Latif, "Acoustic behaviour of 3D printed titanium perforated panels," *Results in Engineering*, vol. 11, Sep. 2021, doi: 10.1016/j.rineng.2021.100252.

[6] A. Barbas, A. S. Bonnet, P. Lipinski, R. Pesci, and G. Dubois, "Development and mechanical characterization of porous titanium bone substitutes," *J Mech Behav Biomed Mater*, vol. 9, pp. 34–44, May 2012, doi: 10.1016/j.jmbbm.2012.01.008.

[7] S. Spigarelli, C. Paoletti, M. Cabibbo, E. Cerri, and E. Santecchia, “On the creep performance of the Ti-6Al-4V alloy processed by additive manufacturing,” *Addit Manuf*, vol. 49, Jan. 2022, doi: 10.1016/j.addma.2021.102520.

[8] J. Lee *et al.*, “Mechanical properties of Ti-6Al-4V thin walls fabricated by laser powder bed fusion,” *Addit Manuf*, vol. 94, Aug. 2024, doi: 10.1016/j.addma.2024.104484.

[9] J. Gockel, J. Beuth, and K. Taminger, “Integrated control of solidification microstructure and melt pool dimensions in electron beam wire feed additive manufacturing of ti-6al-4v,” *Addit Manuf*, vol. 1, pp. 119–126, Oct. 2014, doi: 10.1016/j.addma.2014.09.004.

[10] H. Fan and S. Yang, “Effects of direct aging on near-alpha Ti–6Al–2Sn–4Zr–2Mo (Ti-6242) titanium alloy fabricated by selective laser melting (SLM),” *Materials Science and Engineering: A*, vol. 788, Jun. 2020, doi: 10.1016/j.msea.2020.139533.

[11] S. Sun, M. Brandt, and M. S. Dargusch, “Thermally enhanced machining of hard-to-machine materialsA review,” 2010, *Elsevier Ltd*. doi: 10.1016/j.ijmachtools.2010.04.008.

[12] A. V. S. R. Prasad, Koona. Ramji, and G. L. Datta, “An Experimental Study of Wire EDM on Ti-6Al-4V Alloy,” *Procedia Materials Science*, vol. 5, pp. 2567–2576, 2014, doi: 10.1016/j.mspro.2014.07.517.

[13] R. K. Gupta, V. A. Kumar, C. Mathew, and G. S. Rao, “Strain hardening of Titanium alloy Ti6Al4V sheets with prior heat treatment and cold working,” *Materials Science and Engineering: A*, vol. 662, pp. 537–550, Apr. 2016, doi: 10.1016/j.msea.2016.03.094.

[14] A. Jam, M. Pellizzari, M. Benedetti, C. Gao, M. Vedani, and A. Molinari, “ADDITIVELY MANUFACTURED BETA-TI ALLOY FOR BIOMEDICAL APPLICATIONS,” 2022.

[15] T. S. Tshephe, S. O. Akinwamide, E. Olevsky, and P. A. Olubambi, “Additive manufacturing of titanium-based alloys- A review of methods, properties, challenges, and prospects,” Mar. 01, 2022, *Elsevier Ltd*. doi: 10.1016/j.heliyon.2022.e09041.

[16] M. Galati *et al.*, “Ti-6Al-4V lattice structures produced by EBM: Heat treatment and mechanical properties,” in *Procedia CIRP*, Elsevier B.V., 2020, pp. 411–416. doi: 10.1016/j.procir.2020.05.071.

[17] M. J. Bermingham, D. Kent, H. Zhan, D. H. Stjohn, and M. S. Dargusch, “Controlling the microstructure and properties of wire arc additive manufactured Ti-6Al-4V with trace boron additions,” *Acta Mater*, vol. 91, pp. 289–303, Jun. 2015, doi: 10.1016/j.actamat.2015.03.035.

[18] B. E. Carroll, T. A. Palmer, and A. M. Beese, “Anisotropic tensile behavior of Ti-6Al-4V components fabricated with directed energy deposition additive manufacturing,” *Acta Mater*, vol. 87, pp. 309–320, Apr. 2015, doi: 10.1016/j.actamat.2014.12.054.

[19] M. J. Bermingham, D. H. StJohn, J. Krynen, S. Tedman-Jones, and M. S. Dargusch, “Promoting the columnar to equiaxed transition and grain refinement of titanium alloys during additive manufacturing,” *Acta Mater*, vol. 168, pp. 261–274, Apr. 2019, doi: 10.1016/j.actamat.2019.02.020.

[20] J. Lu and L. Zhuo, “Additive manufacturing of titanium alloys via selective laser melting: Fabrication, microstructure, post-processing, performance and prospect,” Feb. 01, 2023, *Elsevier Ltd*. doi: 10.1016/j.ijrmhm.2023.106110.

[21] B. Dutta and F. H. (Sam) Froes, “The Additive Manufacturing (AM) of titanium alloys,” *Metal Powder Report*, vol. 72, no. 2, pp. 96–106, Mar. 2017, doi: 10.1016/j.mprp.2016.12.062.

[22] Z. Lin, K. Song, and X. Yu, “A review on wire and arc additive manufacturing of titanium alloy,” Oct. 01, 2021, *Elsevier Ltd*. doi: 10.1016/j.jmapro.2021.08.018.

[23] K. Ishfaq, M. Rehman, A. R. Khan, and Y. Wang, “A review on the performance characteristics, applications, challenges and possible solutions in electron beam melted Ti-based orthopaedic and orthodontic implants,” Mar. 18, 2022, *Emerald Group Holdings Ltd.* doi: 10.1108/RPJ-03-2021-0060.

[24] J. D. Cotton *et al.*, “State of the Art in Beta Titanium Alloys for Airframe Applications,” Jun. 11, 2015, *Minerals, Metals and Materials Society*. doi: 10.1007/s11837-015-1442-4.

[25] I. Weiss and S. L. Semiatin, “Thermomechanical processing of beta titanium alloys-an overview,” 1998.

[26] L. Y. Chen, Y. W. Cui, and L. C. Zhang, “Recent development in beta titanium alloys for biomedical applications,” *Metals (Basel)*, vol. 10, no. 9, pp. 1–29, Sep. 2020, doi: 10.3390/met10091139.

[27] M. A. Macias-Sifuentes *et al.*, “Microstructure and mechanical properties of β-21S Ti alloy fabricated through laser powder bed fusion,” *Progress in Additive Manufacturing*, vol. 6, no. 3, pp. 417–430, Aug. 2021, doi: 10.1007/s40964-021-00181-7.

[28] N. Khanna, R. A. R. Rashid, and S. Palanisamy, “Experimental evaluation of the effect of workpiece heat treatments and cutting parameters on the machinability of Ti-10V-2Fe-3Al β titanium alloy using Taguchi’s design of experiments,” 2017.

[29] S. L. Sing, “Perspectives on Additive Manufacturing Enabled Beta-Titanium Alloys for Biomedical Applications,” *Int J Bioprint*, vol. 8, no. 1, 2022, doi: 10.18063/IJB.V8I1.478.

[30] M. J. Bermingham, D. Kent, B. Pace, J. M. Cairney, and M. S. Dargusch, “High strength heat-treatable β-titanium alloy for additive manufacturing,” *Materials Science and Engineering: A*, vol. 791, Jul. 2020, doi: 10.1016/j.msea.2020.139646.

[31] C. H. Ng, M. J. Bermingham, D. Kent, and M. S. Dargusch, “High stability and high strength β-titanium alloys for additive manufacturing,” *Materials Science and Engineering: A*, vol. 816, Jun. 2021, doi: 10.1016/j.msea.2021.141326.

[32] Y. L. Hao, S. J. Li, and R. Yang, “Biomedical titanium alloys and their additive manufacturing,” Sep. 01, 2016, *University of Science and Technology Beijing*. doi: 10.1007/s12598-016-0793-5.

[33] P. J. Bania, “Beta Titanium Alloys and Their Role in the Titanium Industry WHAT IS A BETA ALLOY?”

[34] X. Chen and C. Qiu, “Development of a novel metastable beta titanium alloy with ultrahigh yield strength and good ductility based on laser power bed fusion,” *Addit Manuf*, vol. 49, Jan. 2022, doi: 10.1016/j.addma.2021.102501.

[35] C. Qiu, G. A. Ravi, and M. M. Attallah, “Microstructural control during direct laser deposition of a β-titanium alloy,” *Mater Des*, vol. 81, pp. 21–30, Sep. 2015, doi: 10.1016/j.matdes.2015.05.031.

[36] B. Dutta and F. H. Sam Froes, “The additive manufacturing (AM) of titanium alloys,” in *Titanium Powder Metallurgy: Science, Technology and Applications*, Elsevier Inc., 2015, pp. 447–468. doi: 10.1016/B978-0-12-800054-0.00024-1.

[37] J. Minguella-Canela, S. Morales Planas, V. C. de Medina Iglesias, and M. A. de los Santos López, “Quantitative analysis of the effects of incorporating laser powder bed fusion manufactured conformal cooling inserts in steel moulds over four types of defects of a commercially produced injected part,” *Journal of Materials Research and Technology*, vol. 23, pp. 5423–5439, Mar. 2023, doi: 10.1016/j.jmrt.2023.02.164.

[38] A. T. Silvestri *et al.*, “Assessment of the mechanical properties of AlSi10Mg parts produced through selective laser melting under different conditions,” in *Procedia Manufacturing*, Elsevier B.V., 2020, pp. 1058–1064. doi: 10.1016/j.promfg.2020.04.115.

[39] X. Pan, Z. Tao, and Y. Hong, “Microstructure-based tensile indicator for assessing high-cycle and very-high-cycle fatigue of titanium alloys with additive and conventional manufacturing,” in *Procedia Structural Integrity*, Elsevier B.V., 2025, pp. 1038–1044. doi: 10.1016/j.prostr.2025.06.167.

[40] R. Jones, O. Kovarik, J. Cizek, A. Ang, and J. Lang, “Crack growth in conventionally manufactured pure nickel, titanium and aluminum and the cold spray additively manufactured equivalents,” *Additive Manufacturing Letters*, vol. 3, Dec. 2022, doi: 10.1016/j.addlet.2022.100043.

[41] T. Katagiri, S. Tamura, H. Nozue, and T. Matsumura, “Cutting characteristics of implant materials in milling,” in *Procedia CIRP*, Elsevier B.V., 2022, pp. 397–402. doi: 10.1016/j.procir.2022.06.070.

[42] D. K. Chouhan and S. Biswas, “Multiaxial plane-strain forging and rolling of biomedical grade titanium: Evolution of microstructure, texture, and mechanical properties,” *Mater Lett*, vol. 291, May 2021, doi: 10.1016/j.matlet.2021.129540.

[43] Y. Niu, Z. qiang Hong, Y. qi Wang, and Y. chun Zhu, “Machine learning-based beta transus temperature prediction for titanium alloys,” *Journal of Materials Research and Technology*, vol. 23, pp. 515–529, Mar. 2023, doi: 10.1016/j.jmrt.2023.01.019.

[44] B. Xu, R. Fu, Y. Li, J. Ma, and B. Yan, “Mechanism of α → β dynamic transformation in commercial pure titanium deformed at high temperature below β-transus,” *Mater Lett*, vol. 282, Jan. 2021, doi: 10.1016/j.matlet.2020.128852.

[45] S. Sahoo and S. Roy, “Origin of morphology and orientation of microstructural features in uniaxially deformed Ti-6Al-4V alloys above the β-transus,” *Journal of Alloys and Metallurgical Systems*, p. 100208, Aug. 2025, doi: 10.1016/j.jalmes.2025.100208.

[46] J. Gupta, I. K. Jha, and J. Singh, “Recent advances in the aging of β-titanium alloys,” Apr. 20, 2025, *Elsevier Ltd*. doi: 10.1016/j.jallcom.2025.180098.

[47] Z. Lei, Y. Chen, H. Zhou, X. Wang, J. Liu, and P. Xia, “Melt flow and grain refining in laser oscillating welding of β-21S titanium alloy,” *Opt Laser Technol*, vol. 145, Jan. 2022, doi: 10.1016/j.optlastec.2021.107496.

[48] S. A. Mantri and R. Banerjee, “Microstructure and micro-texture evolution of additively manufactured β-Ti alloys,” *Addit Manuf*, vol. 23, pp. 86–98, Oct. 2018, doi: 10.1016/j.addma.2018.07.013.

[49] S. O. Agbedor *et al.*, “A two-decade odyssey in fusion-based additive manufacturing of titanium alloys and composites,” Aug. 01, 2024, *Elsevier Ltd*. doi: 10.1016/j.apmt.2024.102242.

[50] J. Gumpinger, M. Seifi, N. Shamsaei, C. Seidel, and R. W. Russell, “Recent progress on global standardization,” in *Fundamentals of Laser Powder Bed Fusion of Metals*, Elsevier, 2021, pp. 563–582. doi: 10.1016/B978-0-12-824090-8.00021-4.

[51] S. Lu *et al.*, “Influence of process parameters on the microstructures, residual stresses and mechanical properties of TA15 titanium alloy fabricated by L-PBF,” *Materials Science and Engineering: A*, vol. 927, Apr. 2025, doi: 10.1016/j.msea.2025.147990.

[52] A. Yin *et al.*, “Microstructural and thermal relaxation of residual stress in dual peened TA15 titanium alloy fabricated by SLM,” *Mater Charact*, vol. 218, Dec. 2024, doi: 10.1016/j.matchar.2024.114496.

[53] J. Li *et al.*, “Spatial modulation of eutectoid element in melt pool by EB-PBF for constructing high-performance heterogeneous titanium alloys,” *Addit Manuf*, vol. 110, p. 104948, Jul. 2025, doi: 10.1016/j.addma.2025.104948.

[54] S. E. Haghighi, H. B. Lu, G. Y. Jian, G. H. Cao, D. Habibi, and L. C. Zhang, “Effect of α″ martensite on the microstructure and mechanical properties of beta-type Ti-Fe-Ta alloys,” *Mater Des*, vol. 76, pp. 47–54, Jul. 2015, doi: 10.1016/j.matdes.2015.03.028.

[55] Y. J. Liu, Z. Liu, Y. Jiang, G. W. Wang, Y. Yang, and L. C. Zhang, “Gradient in microstructure and mechanical property of selective laser melted AlSi10Mg,” *J Alloys Compd*, vol. 735, pp. 1414–1421, Feb. 2018, doi: 10.1016/j.jallcom.2017.11.020.

[56] D. Valente Velôso *et al.*, “Additive manufacturing of CAD-CAM complete arch fixed implant restorations supported by six implants: Prosthetic screw stability and marginal precision under masticatory simulation); the Coordination for the Improvement of Higher Education Personnel (CAPES) (Finance Code 001); the National Council for Scientific and Technological Development (CNPq).”

[57] J. Parthasarathy, B. Starly, S. Raman, and A. Christensen, “Mechanical evaluation of porous titanium (Ti6Al4V) structures with electron beam melting (EBM),” *J Mech Behav Biomed Mater*, vol. 3, no. 3, pp. 249–259, Apr. 2010, doi: 10.1016/j.jmbbm.2009.10.006.

[58] M. S. Kenevisi *et al.*, “Tool steels and their additive manufacturing for fabrication and repair via PBF and DED processes: techniques, challenges, and applications,” *Mater Des*, vol. 258, p. 114639, Oct. 2025, doi: 10.1016/j.matdes.2025.114639.

[59] K. Shirasu, T. Mizuno, Y. Hoshikawa, K. Ogawa, Y. Takayama, and H. Tohmyoh, “Experimental and numerical evaluation of the interfacial adhesion properties of additively manufactured carbon-fiber-reinforced thermoplastic/64 titanium hybrids,” *Compos Sci Technol*, vol. 271, Oct. 2025, doi: 10.1016/j.compscitech.2025.111338.

[60] R. Otto, C. Kiener, Y. Küsters, and K. Sørby, “Additive manufacturing of open porous functional structures: Roadmap from manufacturing to the application,” in *Procedia CIRP*, Elsevier B.V., 2022, pp. 334–339. doi: 10.1016/j.procir.2022.09.102.

[61] Y. Du and C. B. Arnold, “Powder melting efficiency during laser powder bed fusion of stainless steel and titanium alloy,” *J Manuf Process*, vol. 120, pp. 161–169, Jun. 2024, doi: 10.1016/j.jmapro.2024.04.046.

[62] L. Portolés *et al.*, “In situ synthesis of titanium alloy powders reinforced with nanoparticles for powder bed fusion: A step towards safer and more sustainable manufacturing,” *Addit Manuf*, vol. 82, Feb. 2024, doi: 10.1016/j.addma.2024.104032.

[63] G. V. Prandi *et al.*, “HYbrid Titanium Alloys produced by laser powder bed Fusion using Ti-5553 and Ti–42Nb powder recycling,” *Journal of Materials Research and Technology*, vol. 27, pp. 8281–8291, Nov. 2023, doi: 10.1016/j.jmrt.2023.11.208.

[64] M. Yamaguchi, K. Kushima, Y. Ono, T. Sugai, T. Oyama, and T. Furumoto, “Humidity control in laser powder bed fusion using titanium alloy powder for quality assurance of built parts and reusability of metal powder,” *J Mater Process Technol*, vol. 311, Jan. 2023, doi: 10.1016/j.jmatprotec.2022.117817.

[65] S. Müller and P. Woizeschke, “Feasibility of a laser powder bed fusion process for additive manufacturing of hybrid structures using aluminum-titanium powder-substrate pairings,” *Addit Manuf*, vol. 48, Dec. 2021, doi: 10.1016/j.addma.2021.102377.

[66] M. H. Mosallanejad, B. Niroumand, A. Aversa, and A. Saboori, “In-situ alloying in laser-based additive manufacturing processes: A critical review,” Aug. 15, 2021, *Elsevier Ltd*. doi: 10.1016/j.jallcom.2021.159567.

[67] S. Chowdhury *et al.*, “Laser powder bed fusion: a state-of-the-art review of the technology, materials, properties & defects, and numerical modelling,” Sep. 01, 2022, *Elsevier Editora Ltda*. doi: 10.1016/j.jmrt.2022.07.121.

[68] P. Ren *et al.*, “Metal powder atomization preparation, modification, and reuse for additive manufacturing: A review,” Jun. 01, 2025, *Elsevier Ltd*. doi: 10.1016/j.pmatsci.2025.101449.

[69] R. K. Gupta, V. A. Kumar, C. Mathew, and G. S. Rao, “Strain hardening of Titanium alloy Ti6Al4V sheets with prior heat treatment and cold working,” *Materials Science and Engineering: A*, vol. 662, pp. 537–550, Apr. 2016, doi: 10.1016/j.msea.2016.03.094.

[70] M. Markl, M. R. Azadi Tinat, T. Berger, Y. Westrich, J. Renner, and C. Körner, “In-situ electron beam characterization for electron beam powder bed fusion,” *Addit Manuf*, vol. 96, Sep. 2024, doi: 10.1016/j.addma.2024.104567.

[71] W. Shen *et al.*, “Surface extraction from micro-computed tomography data for additive manufacturing,” in *Procedia Manufacturing*, Elsevier B.V., 2021, pp. 568–575. doi: 10.1016/j.promfg.2021.06.057.

[72] J. Berglund, J. Holmberg, K. Wärmefjord, and R. Söderberg, “Detailed evaluation of topographical effects of Hirtisation post-processing on electron beam powder bed fusion (PBF-EB) manufactured Ti-6Al-4V component,” *Precis Eng*, vol. 85, pp. 319–327, Jan. 2024, doi: 10.1016/j.precisioneng.2023.10.007.

[73] D. A. Ariza *et al.*, “Development and characterization of Ti-6Al-4V/C103 functionally graded material using LP-DED,” *Addit Manuf*, vol. 109, Jul. 2025, doi: 10.1016/j.addma.2025.104895.

[74] S. Sathiyaraj, S. Venkatesan, S. Ashokkumar, and A. Senthilkumar, “Wire electrical discharge machining (WEDM) analysis into MRR and SR on copper alloy,” in *Materials Today: Proceedings*, Elsevier Ltd, Jan. 2020, pp. 1079–1084. doi: 10.1016/j.matpr.2020.07.123.

[75] L. L. Alhadeff, D. T. Curtis, M. B. Marshall, and T. Slatter, “The application of wire electrical discharge machining (WEDM) in the prototyping of miniature brass gears,” in *Procedia CIRP*, Elsevier B.V., 2018, pp. 642–645. doi: 10.1016/j.procir.2018.08.187.

[76] A. Goyal, “Investigation of material removal rate and surface roughness during wire electrical discharge machining (WEDM) of Inconel 625 super alloy by cryogenic treated tool electrode,” *J King Saud Univ Sci*, vol. 29, no. 4, pp. 528–535, Oct. 2017, doi: 10.1016/j.jksus.2017.06.005.

[77] Z. Chen *et al.*, “A new preparation method of the dual scale surface microstructures with self-cleaning and efficient boiling heat transfer based on wire electrical discharge machining and laser etching,” *Appl Therm Eng*, vol. 279, Nov. 2025, doi: 10.1016/j.applthermaleng.2025.127822.

[78] J. Kozak, K. P. Rajurkar, and N. Chandarana, “Machining of low electrical conductive materials by wire electrical discharge machining (WEDM),” in *Journal of Materials Processing Technology*, Jun. 2004, pp. 266–271. doi: 10.1016/j.jmatprotec.2003.11.055.

[79] V. Lapitskaya, T. Kuznetsova, P. Grinchuk, A. Khabarava, and S. Chizhik, “Micromechanical properties of reaction-bonded silicon carbide using atomic force microscopy and nanoindentation,” *Ceram Int*, vol. 50, no. 24, pp. 52981–52998, Dec. 2024, doi: 10.1016/j.ceramint.2024.10.148.

[80] J. C. Beddoes, R. T. Holt, A. K. Koul, L. Zhao, and W. Wallace, “Lightweight J-l? Immarigeon, Materials for Aircraft Applications.”

[81] D. Monaco, A. Rota, A. Carbonari, E. Lillo, G. M. Lacalandra, and A. Rizzo, “Collection of epididymal semen in the tomcat (Felix catus) by stereomicroscope-aided retrograde flushing (SARF) improves sample quality,” *Anim Reprod Sci*, vol. 261, Feb. 2024, doi: 10.1016/j.anireprosci.2023.107388.

[82] J. J. Orengo-Green, J. Quinto, A. Ricarte, and M. Á. Marcos-García, “Combined stereomicroscope and SEM disentangle the fine morphology of the undescribed larva and puparium of the hoverfly Milesia crabroniformis (Fabricius, 1775) (Diptera: Syrphidae),” *Micron*, vol. 165, Feb. 2023, doi: 10.1016/j.micron.2022.103397.

[83] A. Roslin, D. Pokrajac, and Y. Zhou, “Cleat structure analysis and permeability simulation of coal samples based on micro-computed tomography (micro-CT) and scan electron microscopy (SEM) technology,” *Fuel*, vol. 254, Oct. 2019, doi: 10.1016/j.fuel.2019.05.162.

[84] X. Wang, Y. Chen, L. Yang, D. Li, and H. Zhou, “Investigation of the combined microscopic and macroscopic conditions of magnetic fluids’ magnetoviscous effects at high shear rates in narrow sealing channels,” *J Magn Magn Mater*, vol. 630, p. 173451, Oct. 2025, doi: 10.1016/j.jmmm.2025.173451.

[85] D. Bruce *et al.*, “A critical assessment of the Archimedes density method for thin-wall specimens in laser powder bed fusion: Measurement capability, process sensitivity and property correlation,” *J Manuf Process*, vol. 79, pp. 185–192, Jul. 2022, doi: 10.1016/j.jmapro.2022.04.059.

[86] Y. Yin, S. Huang, Y. Yu, and C. Liu, “Extended application of modified Archimedes’ law in granular media,” *Powder Technol*, vol. 452, Feb. 2025, doi: 10.1016/j.powtec.2024.120560.

[87] M. Ferrucci *et al.*, “Measuring thermal curing induced shrinkage of material extrusion based additive manufacturing silicone elastomer lattices by X-ray computed tomography,” *Tomography of Materials and Structures*, vol. 8, p. 100064, Jun. 2025, doi: 10.1016/j.tmater.2025.100064.

[88] P. J. Withers *et al.*, “X-ray computed tomography,” Dec. 01, 2021, *Springer Nature*. doi: 10.1038/s43586-021-00015-4.

[89] G. Michael, “SPECIAL FEATURE: MEDICAL PHYSICS X-ray computed tomography,” 2001. [Online]. Available: http://iopscience.iop.org/0031-9120/36/6/301

[90] P. Podulka, C. Felho, I. Sztankovics, and L. Knapčíková, “Roughness evaluation of machined Ti-6Al-4V alloys with a study of surface topography measurement noise,” *Measurement (Lond)*, vol. 257, Jan. 2026, doi: 10.1016/j.measurement.2025.118686.

[91] J. Zhang *et al.*, “Microscopic mechanical properties of TiB2/A390 composites studied using in-situ synchrotron X-ray diffraction,” *Journal of Materials Research and Technology*, vol. 38, pp. 1890–1897, Sep. 2025, doi: 10.1016/j.jmrt.2025.07.163.

[92] S. Guo, Q. Meng, X. Zhao, Q. Wei, and H. Xu, “Design and fabrication of a metastable β-type titanium alloy with ultralow elastic modulus and high strength,” *Sci Rep*, vol. 5, Oct. 2015, doi: 10.1038/srep14688.

[93] M. Jafari, M. Vaezzadeh, and S. Noroozizadeh, “Thermal stability of α phase of titanium by using X-ray diffraction,” *Metall Mater Trans A Phys Metall Mater Sci*, vol. 41, no. 13, pp. 3287–3290, Dec. 2010, doi: 10.1007/s11661-010-0393-1.

[94] G. Xu *et al.*, “A review on microstructure design, processing, and strengthening mechanism of high-strength titanium alloys,” Apr. 01, 2025, *Elsevier B.V.* doi: 10.1016/j.pnsc.2025.01.005.

[95] H. Ding *et al.*, “Achieving strength-plasticity synergy in trace B-modified near β titanium alloy fabricated by laser directed energy deposition,” *Mater Des*, vol. 254, Jun. 2025, doi: 10.1016/j.matdes.2025.114082.

[96] C. H. Ng, M. J. Bermingham, and M. S. Dargusch, “Eliminating segregation defects during additive manufacturing of high strength β-titanium alloys,” *Addit Manuf*, vol. 39, Mar. 2021, doi: 10.1016/j.addma.2021.101855.

[97] M. A. Stepanov and S. D. Lavrov, “Modeling nonlinear optical polarization microscopy for visualizing magnetic domain walls,” *Optik (Stuttg)*, vol. 338, Oct. 2025, doi: 10.1016/j.ijleo.2025.172497.

[98] C. jiang ZHANG *et al.*, “Effect of duplex aging on microstructure and mechanical properties of near-β titanium alloy processed by isothermal multidirectional forging,” *Transactions of Nonferrous Metals Society of China (English Edition)*, vol. 32, no. 4, pp. 1159–1168, Apr. 2022, doi: 10.1016/S1003-6326(22)65863-1.

[99] Z. F. Shi, H. Z. Guo, J. Y. Han, and Z. K. Yao, “Microstructure and mechanical properties of TC21 titanium alloy after heat treatment,” *Transactions of Nonferrous Metals Society of China (English Edition)*, vol. 23, no. 10, pp. 2882–2889, Oct. 2013, doi: 10.1016/S1003-6326(13)62810-1.

[100] E. Kim *et al.*, “A guide for nanomechanical characterization of soft matter via AFM: From mode selection to data reporting,” Jun. 20, 2025, *Cell Press*. doi: 10.1016/j.xpro.2025.103809.

[101] M. A. Hasan *et al.*, “Electronic, nanomechanical and smart reversible phase transition behaviours of sputtered titanium oxide-vanadium oxide composite thin films,” *Ceram Int*, vol. 48, no. 23, pp. 35937–35946, Dec. 2022, doi: 10.1016/j.ceramint.2022.10.226.

[102] L. C. Zhang and L. Y. Chen, “A Review on Biomedical Titanium Alloys: Recent Progress and Prospect,” Apr. 01, 2019, *Wiley-VCH Verlag*. doi: 10.1002/adem.201801215.

[103] T. Alves, M. Fetter, C. Busby, R. Gontijo, T. A. Cunha, and N. H. Mattos, “A tectono-stratigraphic review of continental breakup on intraplate continental margins and its impact on resultant hydrocarbon systems,” Jul. 01, 2020, *Elsevier Ltd*. doi: 10.1016/j.marpetgeo.2020.104341.

[104] I. Simsek and D. Ozyurek, “Investigation of the electrochemical corrosion properties of high-energy milled Ti6Al4V alloy in simulated body fluid environment,” *Powder Metallurgy*, vol. 62, no. 3, pp. 169–175, May 2019, doi: 10.1080/00325899.2019.1607029.

[105] S. Kumar and T. S. N. Sankara Narayanan, “Electrochemical characterization of β-Ti alloy in Ringer’s solution for implant application,” *J Alloys Compd*, vol. 479, no. 1–2, pp. 699–703, Jun. 2009, doi: 10.1016/j.jallcom.2009.01.036.

[106] H. Liu *et al.*, “Enhanced corrosion resistance of near β titanium alloy by deep cryogenic treatment,” *Corros Sci*, vol. 255, Oct. 2025, doi: 10.1016/j.corsci.2025.113131.